5-2015

Enhancement of the Performance of GaAs based Solar Cells by using Plasmonic, Anti-Reflection Coating and Hydrophobic Effects

Yahia Fayiz Makableh
University of Arkansas, Fayetteville

Enhancement of the Performance of GaAs based Solar Cells by using Plasmonic, Anti-Reflection Coating and Hydrophobic Effects

Enhancement of the Performance of GaAs based Solar Cells by using Plasmonic, Anti-Reflection Coating and Hydrophobic Effects

A dissertation submitted in partial fulfillment
of the requirements for the degree of
Doctor of Philosophy in Electrical Engineering

By

Yahia F. Makableh
University of Jordan
Bachelor of Science in Mechatronics Engineering, 2009
Georgia Southern University
Masters of Applied engineering, with concentration in Mechatronics, 2011

May 2015
University of Arkansas

This dissertation is approved for recommendation to the Graduate Council

_____
Dr. Omar Manasreh
Dissertation Director

_____
Dr. Simon Ang
Committee Member

_____
Dr. Jingxian Wu
Committee Member

_____
Dr. Jiali Li
Committee Member

Abstract

Investigation of renewable energy resources is gaining huge momentum in recent years due to the limited fossil fuels, and their detriment impact on the environment. Solar energy is promising to meet the increased energy demand. In order to achieve this goal, solar energy has to be harvested efficiently at low cost. Therefore, higher efficiency solar cells are the primary focus of research worldwide. Photovoltaics based on InAs/GaAs intermediate band solar cells and their device performance enhancements are investigated in this dissertation. The device enhancement is carried out by surface modification methods. The dissertation work is inspired by the need of improved efficiency solar cells to meet the new energy demands. In this project, InAs/GaAs intermediate band solar cell and their device performance enhancement are investigated. The device enhancement is carried out though implementing surface modification by using plasmonic effect, anti-reflection coatings and self-cleaning surfaces. Single junction and quantum dots solar cells performance has been unsatisfying due to several optical losses especially high surface reflection. Hence, in this project, potential application of plasmonic effect and significant device performance enhancement implementing anti-reflection coating are studied experimentally. Significantly, GaAs based photovoltaics solar cells efficiencies were improved by 40 – 50 %. In addition, self-cleaning surfaces with contact angle above 156^{o} has been achieved. This self-cleaning surface can ensure proper functionality of the anti-reflection coatings.

Acknowledgments

I would like to express my deep gratefulness to my graduate advisor and dissertation director, Dr. Omar Manasreh to provide me this unique opportunity to perform research in the Optoelectronic and Nanomaterials Lab. His guidance and instructions lead to the hard work achieved in this dissertation. I am very appreciative to Dr. Simon Ang, Dr. Jingxian Wu and Dr. Jiali Li to be part of my committee members, and who made their presence here such a great personal delight. I would like to thank mu great research members, Ramesh Vasan, Ahmad Nusir, Jony Sarker, Seungyong Lee, Mohammed Marie, Sanghamitra Mandal, Rick Eyi, and Juan Aguilar, Kelly McKenzie, Haley Morris and Justin Hill for their support and help throughout my dissertation work. Also, I would like to thank Dr. Min Zou and Dr. Samuel Beckford to offer the contact angle measurements.

This work was supported by the Air Force Office of Scientific Research (Grant No. FA9550-10-1-0136), and NASA (Grant No. 242026-1BBX11AQ36A).

Dedication

This dissertation is dedicated to my parents, my brothers and sisters, my lovely wife and my kids for their help and support to me throughout the course of my studies. Without their valuable advice and wishes I may not have the courage and enthusiasm to continue my PhD program. With all the hard times we went through you were to support me, with all the challenges and difficulties I faced you were there to help me. Here I am today very thankful, and cannot have enough words to describe my feelings towards you for being my greatest supporters no matter what.

Table of Contents

List of Graphs

List of Abbreviations

QD Quantum Dots

ARC Anti Reflection Coating

AM Air mass

I-V Current-voltage

EQE External quantum efficiency

UV-Vis Ultraviolet-visible spectroscopy

XRD X-ray Diffraction

FF Fill factor

ML Monolayer

SPP Surface Plasmon Polaritons

SEM Scanning electron microscopy

MBE Molecular beam epitaxy

I. Introduction

The increased demand on energy usage worldwide, with the increased fossil fuels prices and their negative impact on the environment has inspired many researchers to improve on the solar energy harvesting methods [1]-[4]. The increased interest on solar energy harvesting has promoted more intensive research on both the device structure level and on the devices surface modification [5][6]–[8][9]–[11]. On the device level several structures were investigated and produced such as single junction solar cells [12], intermediate band solar cells and multi-junction solar cells [10], [11], [13]–[16]. Between these different structures intermediate band solar cells implementing quantum dots to the device structure is promising to achieve efficiencies as high as 63 % [16]–[20]. One of the main advantages of using quantum dots solar cells is the ability to achieve bandgap tuning that ranges between the bandgap of the host material (i.e: Eg_{GaAs} = 1.42 eV) and the bandgap of the quantum dots material (i.e: Eg_{InAs} = 1.42 eV) [15], [16], [20]. The ability to band tune the solar cell structure allows extending the solar cell spectral response beyond the host materials bandgap, allowing it to absorb lower energy photons, so the solar cell can reach higher efficiency [1], [21].

On the other hand, being able to grow materials at the nanoscale has introduced new perspectives to enhance the solar cells capacity to absorb light. For example, by using plasmonic nanoparticles [22], anti-reflection coating [23]–[25], surface nanotexturing [26], or any other nanoscale surface modification technique the light reflection is suppressed from around 35 % for materials such as GaAs and Si to less than 0.5 % [27]–[30]. Coupling metallic nanoparticles to the solar cell surface can generate surface Plasmon when stimulated by incident light. This effect is promising to enhance the cell light absorption leading to higher cell efficiency [31]–[33]. Additionally, The capability to control the abrupt change of the refractive index between

air and the solar cell surface by using different materials with refractive indices lies between the two main values (n_{GaAs} = 3.6 and n_{air} = 1) can allow the reflection to be reduced to minimal values [7], [23], [24]. With refractive index tuning the solar cell structure will be able to absorb more photons due to reflection reduction, achieving higher efficiencies.

The focus of this dissertation is to investigate GaAs based photovoltaic devices enhancement. Two approaches are used; the first approach is to introduce InAs/AlGaAs quantum structures to the solar cell device that allows photon absorption at the near infrared region. The second approach is to modify the surface of the solar cell device to achieve low surface reflection.

In chapter 1, operation principle of photovoltaics, review of quantum dots solar cells, plasmonic effect, anti-reflection, and hydrophobic surfaces were discussed. Chapter 2 discusses the solar cells fabrication process and characterizations tools used. Chapter 3 explains the equipment and tools used throughout the dissertation work. Chapter 4 analyses the characteristics and the performance of the InAs quantum dots solar cells. Chapter 5 explains the plasmonic effect on the quantum dots solar cells. In Chapter 6, the anti-reflection coatings effect on the photovoltaic devices performance. Chapter 7 expresses the anti-reflection/hydrophobic dual surface coatings. Finally, in chapter 8, the research contribution, conclusion and future research are presented.

A. Photovoltaics Principle of Operation

Photovoltaic devices are transducers used to convert the solar energy into electricity through the photovoltaic effect [34], [35]. For this effect to take place two main components have to present. The first component is a material that can absorb large portion of the light within

the solar spectrum, in which the absorbed light can generate electron-hole pairs inside the material. The second component is the ability to separate the electron-hole pair before recombination process takes place [36]. Different materials and processes can combine these components in order to have solar energy conversion [37]. Several semiconductors are widely used to absorb the sun light and generate electron-hole pairs while maintaining charge separation before recombination takes place [31]-[34]. Semiconductors such as Gallium Arnside (GaAs), Cadmium Telluride (CdTe), organic polymers, and Silicon solar cells including Crystalline Silicon, Multicrystalline Silicon, Amorphous Silicon and Mono Silicon solar cells are all used in photovoltaic devices. Generally, there are three classifications of solar cells: homojunction p-n diode, heterojunction p-n diode, and Schottky barrier solar cells [38]. Both homojunction and heterojunction solar cells are most used nowadays for solar energy harvesting [39], [40]. In any type of solar cell, the built in electric field will provide separation between the electrons and holes, deriving the electrons to the n side and the holes to the p side of the solar cell [36], [41]. The simplest representation of pn junction solar cell is by using the ideal diode model. The ideal diode model and the IV characteristics of both ideal solar cell and real solar cell are shown in figure 1.1.

To represent the solar cell current-voltage (I-V) characteristics the ideal diode representation can be used. The ideal diode current equation is [42]:

$$I = I_o\left[\exp\left(\frac{qV}{nkt}\right)-1\right] \tag{1-1}$$

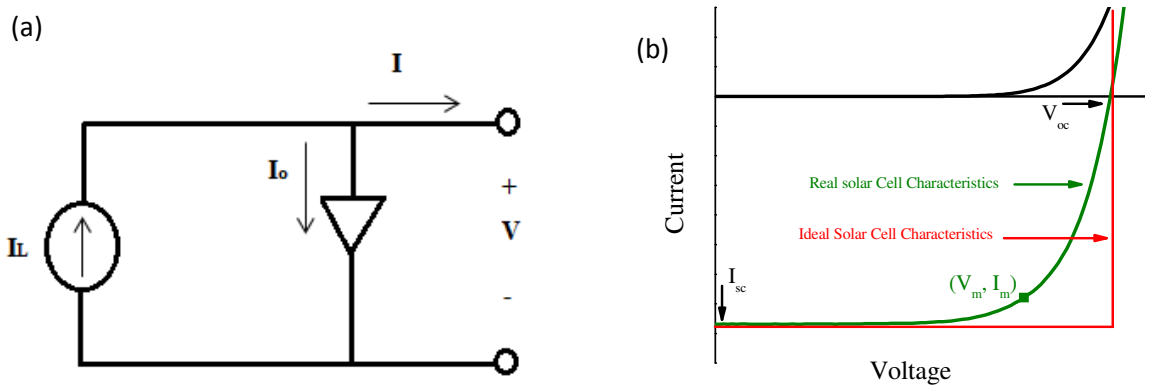

Figure 1.1. (a) Diode circuit (b) Current-Voltage characteristics of real solar cell compared to ideal solar cell

where I_o is the saturation current, V is the applied voltage, q is the electron charge, k is the Boltzmann's constant, T is the absolute temperature, and n is the ideality factor. When the sunlight shine on the solar cell electron hole pairs will be generated, the generated pairs forms a current (photocurrent), that is in reverse direction with the dark current, hence the diode equation can be modified to include the photocurrent (I_L) [41], [42]:

$$I = I_L - I_o\left[\exp\left(\frac{qV}{nkt}\right) - 1\right] \tag{1-2}$$

From the solar cell I-V characteristics, three important parameters can be extracted:

1. The open circuit voltage (V_{oc}): The maximum voltage can be generated at zero current.
2. The short circuit current (I_{sc}): The maximum obtained output current at zero voltage.
3. Maximum output power (P_m): The highest output power can be obtained from the solar cell under illumination.

For an ideal solar cell, the maximum output power will be equal to 100 %, which will require the solar cell to operate at the short circuit current, and the open circuit voltage at the same time [16], [41], [42]. This condition cannot be satisfied in practical solar cells; henceforth the maximum output power will always be less than 100 %. Additionally, from the solar cell I-V characteristics curve, more valuable information can be obtained such as the Filling Factor (FF) and the power conversion efficiency (η), which are measure of the solar cell quality and performance. The values of both the filling factor and the power conversion efficiency can be written as the following [42]:

$$FF = \frac{V_m I_m}{V_{oc} I_{sc}} \tag{1-3}$$

$$\eta = \frac{P_m}{P_{in}} \times 100\% = \frac{V_m I_m}{P_{in}} \times 100\% \tag{1-4}$$

where P_{in} is the solar cell input power, which equals to 135.5 mW/cm^2 just above the surface of earth.

Both the filling factor and power conversion efficiency give important information about the cell. The filling factor is related to the solar cell quality in terms of junction quality and parasitic resistance. The closer filling factor to unity is the better solar cell. Likewise, the power conversion efficiency is the ratio between the output power to the input power. The ideal power conversion efficiency will be 100 %, but a practical solar cell will have less than 100 % value. Since the solar cell efficiency relies on the sunlight (input power) the solar cell needs to absorb the maximum amount of photons in its spectral range [43], [44]. Thus, any incident photons

with energy less than the solar cell bandgap will not get absorbed in the cell materials, so it cannot generate any electron-hole pairs. Moreover, the cell surface will reflect portion of the incident light, eliminating another part of the sun energy to be wasted without being absorbed via the cell [12], [45]–[47].

Gallium Arnside and Indium Arsenide Quantum Dots Solar Cells

Gallium Arsenide solar cells gained importance as photovoltaic devices since they can be grown as thin films, their wide spectral range, high photon absorption, low surface recombination, low series resistance, higher mobility and longer minority carriers life time and diffusion lengths [48], [49]. These characteristics made GaAs single junction solar cells to reserve the world record as the highest single junction solar cell efficiency of about 28 %, compared to Si solar cells single junction solar cells highest reported efficiency of about 25 % [38]. Moreover, GaAs has high absorption coefficient making it an excellent choice to be grown as thin films solar cells, as around 95 % of the incident photons can be absorbed in very thin layer as low as 3µm length [49], [50]. For GaAs the calculated theoretical efficiency can be on the order of 39 %, yet this efficiency is not achieved [11], [30], [41], [43].

On the other hand, the device structure of GaAs solar can be altered by introducing other material to it such as InAs. The introduction of InAs to the structure of GaAs allows bandgap tuning due to the lower bandgap of InAs (~ 0.38 eV) and GaAs bandgap (~ 1.42 eV) [9]. This can be achieved by growing quantum structures (quantum dots in the in InAs case), allowing high quantum confinement in these structures, hence the ability to reach higher efficiencies compared with only p-n junction solar cell [10], [11], [17], [18], [20], [42]. Indium Arsenide quantum dots solar cells are one type of intermediate band solar cells. These solar cells have the

ability to extend the spectral response of the host semiconductor material bellow the bandgap, allowing the solar cell to absorb photons with energies bellow the bandgap of the host materials. Therefore, achieving higher efficiencies. This is possible due to the quantized energy levels that the quantum dots add to the structure, making it able to absorb lower energy photons [9], [16], [42].

The theoretical limit of intermediate band solar cells can be as high as 63 % as reported by A. Marti and A. Luque in their theoretical calculations for this type of solar cells [16], [17]. In spite of the expected high efficiency for intermediate band solar cells, there are several drawbacks of using them, limiting these solar cells from achieving high efficiency [9]–[11], [14]. The light absorption of quantum dots is very low due to their small size, so several layers with different sizes have to be grown to enhance the light absorption. Using different layers of quantum dots can cause high strain between the different grown layers due to the lattice mismatch between them and the host material, making the InAs quantum dots solar cells fail to reach the expected high efficiency[14], [15], [19], [20].

Although GaAs single junction and InAs quantum dots solar cells have promising theoretical efficiencies, they suffer from several losses reducing their capacity to reach high performance and to be used in mass production, some of these limitations are [7], [12], [30], [51]–[53]:

1. Optical losses. The optical losses are one of the most type of loses that affect the solar cell performance. Some of these losses are: photons reflection from the solar cell surface, low energy photons that falls below the cell bandgap, radiative recombination, and light absorption from inactive layers and metal contacts.

2. Lattice Thermal losses. Thermal loses include non-radiative combination of generated electron hole pairs in defects, junction losses, and relaxation of the electron hole pairs to their bands before being collected.
3. Electrical loses. Electrical loses include contact loses, front and back surface recombination, and solar cell internal resistance.

Between the different types of losses; solar cell reflection loses can be considered the most important one. For example, GaAs solar cell surface can reflect as much as 35 % of the indicant light due to the high GaAs refractive index (~ 3.6) [30], [52]. Solving the light reflection problem is under intensive research worldwide in order to lower the reflection to values below 1 %, which leads to high improvement on the solar cell performance. Some of the methods used are anti-reflection coatings [12], [45], [47], [54], [55], surface Plasmon [22][56]–[59], and nanotexturing [26].

B. Plasmonic Effect

Current solar cells materials and technologies still suffer from absorbing the photons at the materials bandgap leading to lower cell efficiency. This is limiting solar cells from reaching their optimum performance to meet the new energy demands. Therefore, new techniques and materials must be developed to help solar cells gain productivity. For this purpose light trapping though plasmonic effect is gaining more attention [60]. This phenomena was first explained by Rufus Ritchie in 1959, where it was reported a loss of electron in thin film materials, that was a hint about Plasmon mods can be produced in a metal surface [61]. A demonstration of surface collective excitations and the quanta of surface waves was then followed by Powell and Swan in their work investigating electron energy losses in both Aluminum and Magnesium [62], [63].

For Plasmon, generally it is classified as bulk Plasmon, surface Plasmon and localized surface Plasmon.

Bulk Plasmon can be explained as collective oscillations of free electrons, where the electrons are unbound, and they oscillate with respect to applied electromagnetic field. The frequency of the electrons oscillation are represented as [64], [65]:

$$\omega_p = \frac{ne^2}{\varepsilon_0 m} \tag{1-5}$$

where n is the electron density, e is the electron charge and ε_0 is the electric permittivity.

According to Maier, the dielectric function of the free electron gas can be written as [64]:

$$\varepsilon(\omega) = 1 - \frac{\omega_p^2}{\omega^2 + i\gamma\omega} \tag{1-6}$$

from which the relationship can be written for frequency approaching plasma frequency ($\omega >> \gamma$) as:

$$\varepsilon(\omega) = 1 - \frac{\omega_p^2}{\omega^2} \tag{1-7}$$

From this relationship, for a traveling transverse electromagnetic field the dispersion relationship can be obtained as in Drude model as:

$$\omega^2 = \omega_p^2 - K^2 c^2 \tag{1-8}$$

Taking the case where $\omega = \omega_p$ then both K , c are zero. Hence, at the frequency equals the plasma frequency, the bulk Plasmon will correspond to a collective oscillation along the

longitudinal direction of the free electrons. With a manner similar to bulk Plasmon, the surface Plasmon polartion (SPP) can be explained as the electrons oscillations restrained at a metal-insulator interface. To represent the SPPs with mathematical equation, first assume the z-plan has no spatial variations, and the y direction is a function of $\varepsilon = \varepsilon(z)$, then the wave function can be written as:

$$\frac{\partial \mathrm{E}(z)}{\partial z^2} + \left(k_0^2 \varepsilon - \beta^2\right)\mathrm{E} \tag{1-9}$$

where $k_0 = \frac{\omega}{c}$ which is the wavenumber of electromagnetic field in vacuum and β is the wave vector in the direction of plasma propagation. By the application of Maxwell's equation the wave function can be written as:

$$\frac{\partial H(y)}{\partial z^2} + \left(k_0^2 \varepsilon - \beta^2\right)H_y = 0 \tag{1-10}$$

from which the propagation wave vector at the interface can be written as

$$\beta = k_o \sqrt{\frac{\varepsilon_1 \varepsilon_2}{\varepsilon_1 + \varepsilon_2}} \tag{1-11}$$

where ε_1 is the metal permittivity and ε_2 is dielectric permittivity. The frequency of the SPPs approaches the Plasmon frequency at high values and can be written as:

$$\omega_{sp} = \frac{\omega_p}{\sqrt{1 + \varepsilon_2}} \tag{1-12}$$

On the other hand, the localized surface plasmin (LSP) can occur in metallic nanoparticles as a non-propagating electron oscillation. In metallic nanoparticles the excitation wavelength is smaller than regular bulk materials case. Thus the oscillation can be assumed as harmonic and constant. With this assumption, the quasi-static approximation can be used to determine the electromagnetic wave. To get the mathematical representation, the plasmonic nanoparticles can be assumed to have spherical shape with radius a, as shown in figure (1.2).

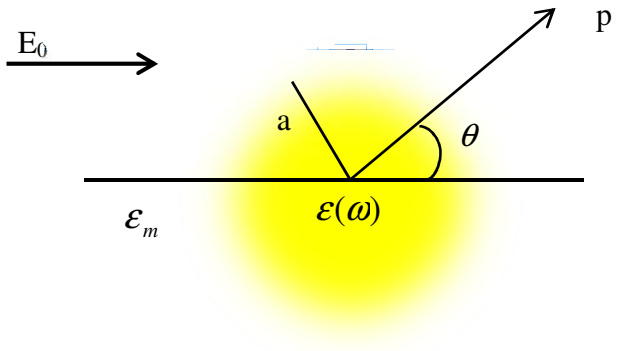

Figure 1.2. Schematic of spherical shape metallic nanoparticle with radius equals a

The dielectric constant of the medium around the nanoparticles will be ε_m and for the nanoparticle itself is ε_ω. With a uniform electric field ($\mathrm{E}_o = E_o\varepsilon$) the nanoparticle can be found in, the interaction can be found by solving the Laplace equation for electric potential:

$$\nabla^2\Phi = 0 \tag{1-13}$$

Both in and out potentials of the nanoparticle can have general solutions as [66], [67]:

$$\Phi_{in}(r,\theta) = -\frac{3\varepsilon_m}{\varepsilon + 2\varepsilon_m} E_o r\cos\theta \tag{1-14}$$

$$\Phi_{out}(r,\theta) = -\Phi E_o r\cos\theta + \frac{\varepsilon - \varepsilon_m}{\varepsilon + 2\varepsilon_m} E_o a^3 \frac{\cos\theta}{r^2} \tag{1-15}$$

where Φ_{in} and Φ_{out} are the potentials inside and outside the nanoparticles, respectively. With assuming the nanoparticle as an ideal dipole under the quasi-static conditions, the electric fields can be written as [64]:

$$\mathrm{E_{in}} = \frac{3\varepsilon_m}{\varepsilon + 2\varepsilon_m} E_o \tag{1-16}$$

$$\mathrm{E_{out}} = E_o + \frac{3n(p.n) - p}{4\pi\varepsilon_o\varepsilon_m r^3} \tag{1-17}$$

and polarization (α) of the metallic nanoparticles can be written as [64]:

$$\alpha = \frac{P}{\varepsilon_o\varepsilon_m E_o} = 4\pi a^3 \frac{\varepsilon - \varepsilon_m}{\varepsilon + 2\varepsilon_m} \tag{1-18}$$

From these equations it can be noted that when $|\varepsilon + 2\varepsilon_m|$ minimum, all of the fields and the polarization are will be at maximum values. From this, the resonance condition Re[$\varepsilon(\omega)$] = $2\varepsilon_m$ relates to both the internal and the dipolar fields, which has field enhancement at the resonance, making metallic nanoparticles a best choice for several optoelectronic and optical applications [64].

C. Anti-Reflection Coating

One of the major optical loses the solar cell device suffers from is the reflection of incident photons from the device surface [45], [54]. This problem is responsible about lowering the cell photocurrent generation, leading to lower power conversion efficiency. Different

techniques are being under study to investigate their effect on lowering the photon reflection. For example using InAs quantum dots or mutli-junction solar cells can enhance the photon absorption at different photon energies. While these methods can lead to reasonable power conversion improvement, they do not offer the best solution for the reflection issues. In order to better reduce the reflection to values close to zero (achieving destructive interference) a smooth change of the refractive index between air and the solar cell material refractive index must occur [27]–[30]. As a result choosing anti-reflection coating (ARC) as the solution for the reflection problem is the most suitable choice. This can be achieved by coating the cell surface with thin dielectric materials of suitable refractive index to reach that point of smooth refractive index change. This method can be implemented by using one single coating in which the material to be used should have a refractive index value as described in the equation below [68]:

$$n_{ARC} = \sqrt{n_{GaAs} n_{substrate}} \tag{1-19}$$

where n_{air} the refractive index of air which is equals to one, and $n_{substrate}$ is the solar cell substrate refractive index, in this case is the refractive index of GaAs (~ 3.6). A schematic showing the light reflection of a solar cell surface is shown in figure 1.3.

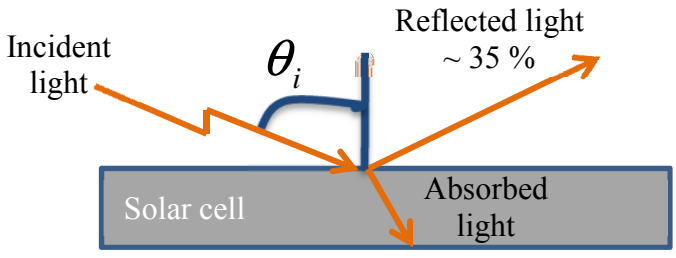

Figure 1.3. Schematic showing light reflection from solar cell surface

Two main parameters are involved in the ARC process. The first parameter is the selection of the refractive index as mentioned above. Here, to keep in mind that if the ARC consist of more than one material in different layers, then the top layer should have lower refractive index than the materials bellow it, this has to be maintained to insure smooth change of refractive index between n = 1 for air and n = 3.6 as in GaAs substrate [23]. The second parameter in the ARC design is the thickness of each layer. For GaAs solar cells, the main spectral range falls between 400 nm to 800 nm. Thus, the total thickness of the ARC layers should stay equal or less than one forth the wavelength of interest according to the following equation [68]:

$$d = \frac{\lambda}{4n_{ARC}} \tag{1-20}$$

Single coating and multi ARC have been used for different solar cells [23], [69]. For example the blue color found on Si solar cells is related to the SiN ARC layer deposited on Si by using plasma enhanced chemical vapor deposition [70]. Schematic showing the bilayer ARC method is shown in figure 1.4. Also, different coatings have been reported to be used on GaAs such as using ZrO_2/Al_2O_3 bilayer and TiO nanocolumns single layer coating[12], [54]. Quite a few methods are used to deposit ARC on solar cells; some of these methods are sputter deposition of oxides, chemical vapor deposition, sol-gel, chemical hydrothermal growth and many other methods. This project focuses on using sol-gel based oxides and hydrothermal growth of oxide nanostructures.

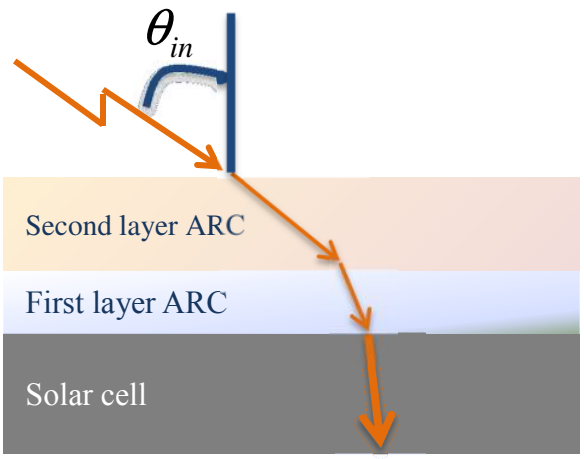

Figure 1.4. Bilayer anti-refection coating schematic

D. Hydrophobic Surface Modification

Hydrophobic surface or self-cleaning surface is a surface that has water (or liquids) repellency properties [71], [72]. This kind of surface can be obtained by reducing the surface tension energy from high surface tension to low surface tension [5], [72], [73]. The result from this transformation is surface with non-sticking feature. Water resistant surfaces have gained wide attention between research groups due to large number of applications. For example, this surface is highly desired in vehicles windshields, in order to repel the water from their surface and get good vision back as quickly as possible. This type of surface feature is highly desirable in photovoltaics applications as they can eliminate the need of glass packaging and also to keep the solar cell panels clean specially in remote places to maintain high light transmission[72], [74]–[76]. Thus far finding a surface with superhydrophobic characteristics and having excellent light transmission properties has been a challenge in the photovoltaic field.

There are three cases a water droplet can face when touching a solid surface. The first case is that the water droplet spreads over the surface and fills all air gaps that can be found on

the surface, or what is called hydrophilic surface. The second case is that the water droplet forms a spherical shape that somehow sticks to the surface and does not allow the water droplet to roll away. This case when the surface is on the limit between hydrophilic and hydrophobic (Wenzel state) [77]. The third case is when the water droplet forms a sphere that rolls away and does not stick to the solid surface. This last case is the hydrophobic surface (Cassie-Baxter case) [77]. A schematic showing interfacial tensions faced by a water droplet on a solid surface is shown in figure 1.5. The most important parameter that defines these stats is the liquid-solid contact angle. The higher the contact angle is the more hydrophobic and less hydrophilic surface. The contact angle was first defined in 1805 by Thomas Young as the following [78]:

$$\gamma_{SG} = \gamma_{SL} + \gamma_{LG} \cos\theta_{CA} \tag{1-21}$$

where γ_{SG}, γ_{SL} and γ_{LG} are the interfacial tension between solid-gas, solid-liquid, and liquid-gas, respectively. The contact angle measurement θ_{CA} is the parameter used to define the droplet state and can be measured with contact angle goniometer.

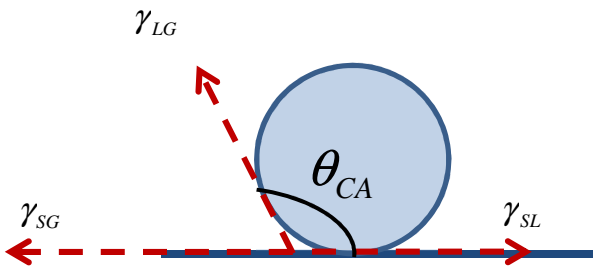

Figure 1.5. Interfacial tension forces a water droplet faces when in contact with a solid surface

The state transfer between hydrophilic to hydrophobic or change from Wenzel state to Cassie-Baxter state happens is when a water droplet does not fill the air gaps in a micro-structured surface [72], [77]. The water droplet in this case has to maintain its shape and can repel itself from the surface easily.

II. Research Methodology

A. Introduction

In this study, Gallium Arsenide based solar cells and their device performance enhancement by using surface modification are investigated. The solar cell fabrication and the surface modification materials growth will be discussed. The solar cells wafers growth has been done using Molecular Beam Epitaxy, and is expressed in section B. The solar cell device fabrication has been using standard industrial photolithography, and discussed in section C Chemical growth methods have been followed to grow the surface modification materials and expressed in section D. Moreover, the characterization tools used in this project are also discussed in this chapter in section E.

B. Epitaxial Growth of GaAs Wafers and Quantum Dots

Molecular Beam Epitaxy (MBE) is an advanced growth tool that is used in high quality semiconductors wafers. The ability of the MBE tool to reach ultra-high vacuum (10^{-10} torr) allows particle free environment needed for high quality growth. In general, the sources are introduced to the chamber through heated effusion cells. When the materials provided get heated they evaporate into the chamber, and when in contact with the wafer substrate they stick to it making layers stacked on top of each other. By using MBE a controllable 1-2 monolayers/second can be achieved, so the deposition process and each layer thickness can be highly controlled. Usually several in-situ characterization tools are integrated with the MBE tool allowing high quality control during the growth process. In this study, both GaAs p-n junction reference wafers, and InAs quantum dots in InGaAs quantum well wafers were grown by using MBE technique implementing Stranski-Krastanov method.

Three different methods are mainly used in epitaxial growth. These methods are Stranski-Krastanov (SK), Frank-Van de Merwe (layer mode) and Volmer-Weber methods (island mode). The SK method is a combination between the other two methods which are island mode and layer mode, and this method was used to grow the quantum structures used in this project wafers. In these wafers a wetting layer consisted of 2-3 monolayers of InAs are grown on GaAs buffer layer. Three dimensional islands were grown over the film in order to release some of the strain that occur between GaAs and InAs due to lattice mismatch. The formation of these three dimensional island forms the InAs quantum dots, where each island may form different size of quantum dots than the other islands. The size and density of the quantum dots can be controlled by changing the MBE growth conditions.

In this project, the GaAs solar cell structures were grown by using MBE on GaAs (100) epi-ready wafers. The structures were grown on an n-type substrate doped with [Si] = 2×10^{18} cm^{-3}. The p-type side of the GaAs was doped with [Be] = 5×10^{18} cm^{-3}. A 100 nm n-type $Al_{0.85}Ga_{0.15}As$ barrier was inserted in the buffer layer, and 100 nm p-type $Al_{0.15}Ga_{0.85}As$ barrier was inserted in the cap layer. These AlGaAs barriers are introduced as fence barriers to reduce the charge trapping effect. For the quantum dots in quantum well growth, ten periods of 2ML/35 nm InAs quantum dots/5 nm of $In_xGa_{1-x}As$ quantum well/35nm and GaAs as a barrier, where x is the Indium mole fraction, and was changed between 0 – 25 %. A schematic representing the general device structure is shown in Figure 2.1

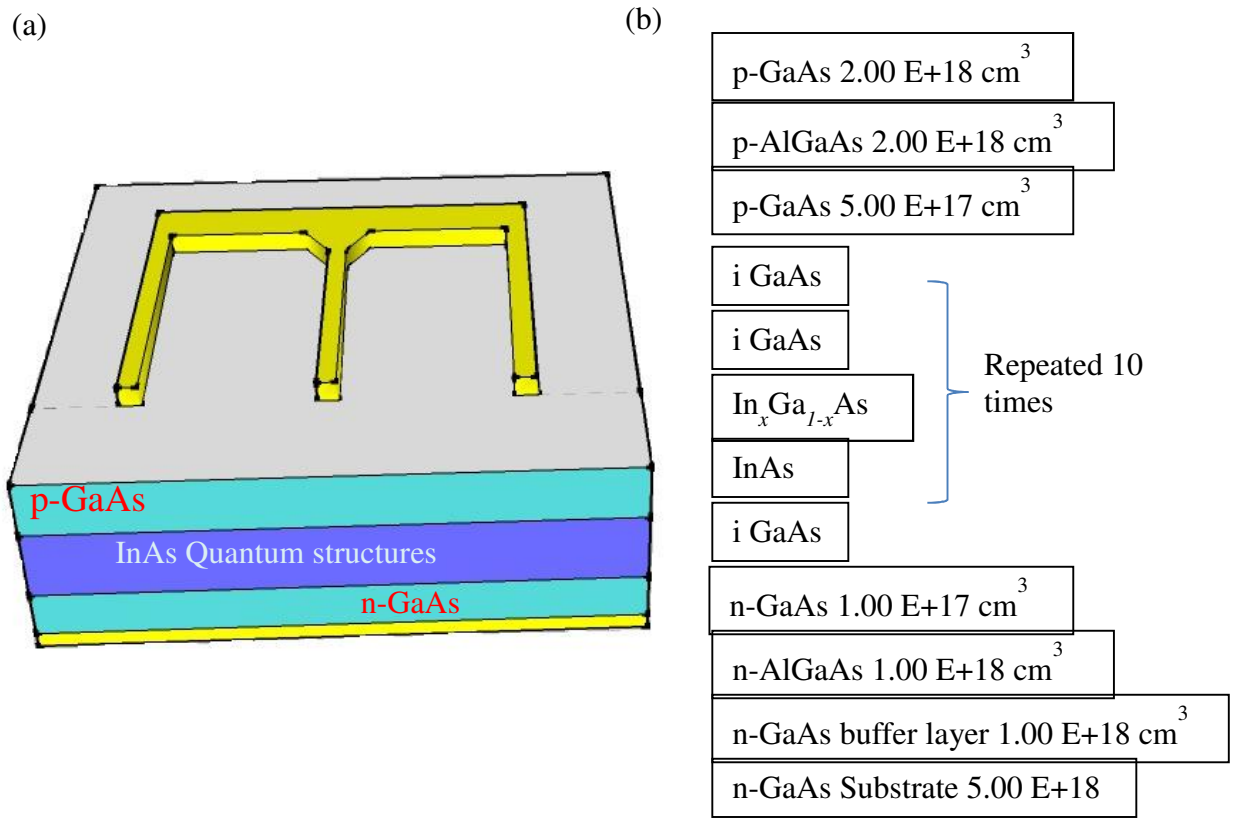

Figure 2.1. (a) Solar Cell Schematic. (b) Solar Cell device structure.

C. Solar Cells Device Fabrication

The solar cells fabrication is done in class 100 clean room, by using established industrial standard photolithography procedures. The solar cell fabrication uses a 3 X 3 mm mesa. The detailed procedure is explained in the following steps:

1. Sample Cleaning: The sample cleaning follows dicing the MBE grown wafers into smaller parts. Usually each sample can form 6 – 8 devices, with each device formed from 3 X 3 mm mesa. The cleaning process is done by soaking the samples into Acetone followed by Methanol then Isopropyl Alcohols for three minutes in each solvent. These solvents can ensure removal of the organic contamination from the sample surface.

2. Photolithography. In this step a two mask process is followed. First positive photoresist AZ® P4330 is spin coated on the sample at 3000 rpm for 60 seconds, and then the sample is baked at 110 ^{o}C to ensure uniform photoresist film. After baking a pattern from a photomask is transferred to the photoresist using UV light station and developed using AZ® 400K. The samples then etched using GaAs etchant that contains H_2O_2:H_3PO_4:H_2O with concentration 3:1:100. This chemical etcher gives around 100 nm per minute rate, so the samples can be immersed for calculated times depending on the required thickness. After etching the sample is washed with DI water in order to stop the etchant effect, then cleaned with Acetone to remove the excess photoresist in order to check the etched thickness by using a Taylor Hobson 3D optical profiler. The second step is to pattern the formed mesas by using a second mask to transform the metal contact shapes. Just before coating the sample with photoresist for the second step, the sample is cleaned with solvents again then immersed in 6 % HCL solution to make sure any surface oxides are removed before metallization.
3. Metallization. The metal contact for both the n-type and p-type contacts are grown using Angstrom Nexdep electron beam evaporator. Before deposition the electron beam chamber is pumped down to $2x10^{-7}$ torr vacuum level. The n-type metal contact is formed using AuGe/Ni/Au 75/30/100 nm, respectively. The p-type metal contact is formed using Au/Zn/Au 30/30/100 nm, respectively. Throughout the deposition process the substrate temperature was held at 100 ^{o}C in the e-beam chamber to allow diffusion of the metals into the device surface to have high quality Ohmic contact. The metals deposition rate was varied between 1 – 2 Angstroms per second. Then, after the metallization of the top contact is finished a left off step is performed in order to remove

the excess materials from the top surface. A schematic showing the fabrication process is shown in figure 2.2.

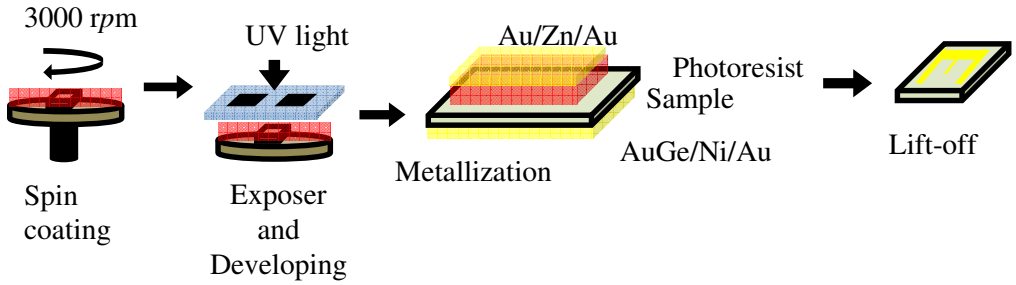

Figure 2.2. Fabrication Process schematic

D. Plasmonic Nanoparticles Growth

Two different methods were followed to grow the plasmonic nanoparticles. In the first method colloidal chemical growth was used [79], [80]. The second method was using e-beam deposition of both Ag and Au.

Plasmonic Nanoparticles Synthesis by Colloidal Growth

1. Silver Nanoparticles Colloidal Growth

To synthesize Ag colloidal nanoparticles Silver Nitrate was used as a precursor. First a 15 mL of 30 mM $AgNO_3$ was prepared with Toluene. The solution was set at an ice cold temperature while stirring at 400 rpm. Meantime, a 0.4 M Sodium Bromide 8 ml solution was prepared in Toluene also. The addition of $NaBH_4$ to the Toluene was very slowly whole at low temperature and stirring, not to oxidize the Sodium Bromide. Both Solutions were pre mixed for 30 minutes, and then the $NaBH_4$ was added to the $AgNO_3$ solution slowly while keeping the same conditions. The total mixture is stirred for two hours, it is mentioned that the solution color turns to green color. After stirring finished the solution was set to rest to separate the organic

phase from it. After organic phase separation the solution was washed several times with DI water.

2. Gold Nanoparticles Colloidal Growth

The synthesis of the Au was carried out in the same manner as the synthesis of Ag nanoparticles, except that the medium was DI water rather than Toluene. In this process a 0.7074 g of Au (III) chloride was dissolved in 60 ml DI water, and set to stir at room temperature at 400 rpm. Meanwhile, another solution was prepared in 160 ml Toluene containing 7.374 Tetraoctyl Ammonium Bromide (TOAB), this solution is premixed for 30 minutes at 400 rpm as well, and cooled down to ice cold temperature. Both solutions were then mixed together and stirred for another 30 minutes. A third solution contains 0.72 NaBH4 in 50 ml of ice cold DI water was prepared. The Sodium Bromide solution was then added to the first mixture slowly and kept stirring at ice cold temperature for 20 minutes. With time the total mixture started to get red in color, which is where the gold (III) transfers to nanoparticles gold (0). Similar to the Ag nanoparticles synthesis, the solution was set to rest to separate the organic phase, followed by washing with DI water several times.

Plasmonic Nanoparticles Growth by E-beam Deposition

Electron beam deposition of metallic nanoparticles was carried out to deposit both Au and Ag nanoparticles. In this process Angstrom NexDep e-beam was used. This system can reach deposition rates as low as 0.25 A^o per second. The deposited layers had total thicknesses between 0.5 nm to 2 nm. The deposition was completed at room temperature, after reaching 2 x 10^{-7} torr. Since the both the deposition rate and the deposited thicknesses were very low, high vacuum level was required to have good control over the deposition process. Glass and GaAs

were used as the deposition substrates. The glass substrate was needed to study the metallic nanoparticles absorption spectra. While the GaAs substrate was used to study the plasmonic effect on GaAs transmission. Post annealing is followed for all samples at varied temperatures to study the effect of annealing on the plasmonic nanoparticles. Further discussion about the results obtained is in the following chapters.

E. Growth of Anti-Reflection Coatings Compounds

Several methods have been used to synthesize ARC materials. The focus of this project is on the sol-gel method. The sol-gel approach is preferred over others due to the lower cost, ease of process, low toxic materials, and the ability to optimize the method to obtain higher quality sol-gels [27], [29]. In this method, metal alkoxides or inorganic slats are used as precursors. Condensation and hydrolysis reactions occur on the precursor mixed with a catalyst inside a solvent medium. For example Zinc Oxide sol gel can be synthesized as follows [81], [82]: First a 0.5 molar of zinc acetate in 2-methaexethanol is prepared by dissolving 0.010975 gm zinc acetate in 10 mL 2-methaexethanol. The mixture is set to stir at 400 rpm at 65 ^{o}C for one hour (milky white solution is observed). Then Monoethanolamine is added to the solution maintaining same molarity, while keeping the mixture on same condition for another hour. The addition of Monoethanolamine is used to stabilize the ZnO solution and to enhance the solvability of all the Zinc Acetate in the solvent, after this step the solution turns into clear transparent solution. The solution then transferred to sonication system and kept there at 65 ^{o}C under sonication for 90 minutes. After sonication the solution is aged foe 24 hours before use. In this project several sol-gels have been prepared and investigated such as ZnO, TiO_2, SiO_2, and ZnS. Additionally, MgF_2 has been investigated but by using ebeam deposition for it.

Hydrothermal Growth of ZnO Nanostructures

The ability to synthesis oxide based materials in nanoscale has several advantages over using bulk film coatings. For example ZnO can be grown as nanowires and nanocrystals, TiO_2 can be synthesized as nanocolumns and SiO_2 can be grown as nanoparticles in different sizes. All of these possibilities give the ability to tune the change in refractive index using only one type of materials such as using ZnO nanoneedles [83]. Another approach can be done by using two different types of nanoshapes such as using ZnO or TiO_2 nanorods and decorating their top with SiO_2 nanoparticles. Moreover, the increase of surface roughness by suing these nanostructures will allow the modified surface to be treated for hydrophobicity compared to only film coating or no coating situations, by using fatty acids [84], [85]. The results and discussion of superhydrophobicity are expressed in later sections.

Hydrothermal growth method is used in this study to grow ZnO nanoneedles on top of the solar cells [86]–[90]. In this method, the solar cell first is coated with a thin layer of ZnO sol-gel acting as a seed layer to start the growth process. The growth solution is prepaid by preparing 0.025 molar Zinc Nitrate solution, and 0.025 molar HTMA solution both in DI water. The two solutions were premixed to dissolve all salts particles in the DI water. Then the two solutions are mixed together and stirred for 90 minutes. In order to obtain nanoneedles shape the pH of the mixture is raised up to 10 by using ammonium hydroxide. After the mixing step the coated solar cells are then immersed in the solution and placed in a closed oven at 90 ^{o}C for 3 hours until the growth process is finished. Figure 2.3 shows the flowchart of the hydrothermal growth process.

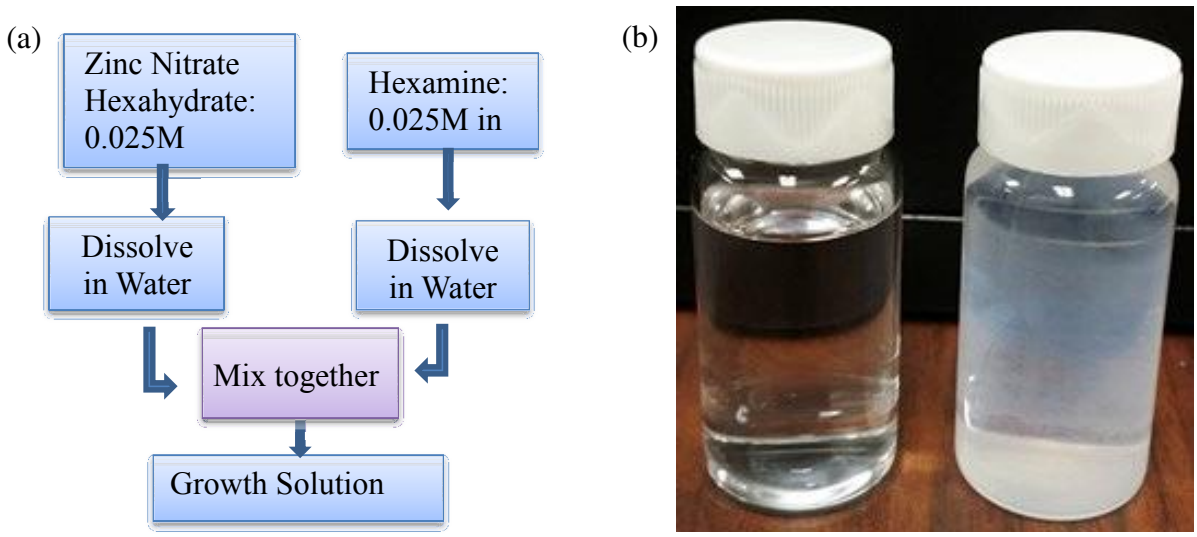

Figure 2.3. (a) Flow chart of ZnO nanorods growth. (b) Change of color of ZnO nanorods growth solution after growth process completed "Photo by Yahia Makableh".

F. Hydrophobic Surface Treatment

One of the main challenges solar cells face beside the reflection problem is blocking part of the incident light to it that could be due to accumulated dust and dirt on top of the solar cell. In order to maintain clean surface that passes all the incoming light a superhydrophobic surface has been introduced to the solar cells. Hydrophobicity or self-cleaning is the ability of a surface to repel water from it. During the water repellency process a high chance of all surface contaminants to be cleaned is possible. In general there are three cases of water contact angle relative to the surface that defines weather the surface is hydrophilic, hydrophobic or superhydrophobic [5], [72], [73].

In this project superhydrophobicity has been achieved by treating the surface of ZnO nanoneedles with fatty acid called Stearic Acid. This acid has the longest carbon chains among all other types of acids, and is not toxic as it is obtained from animal's fat [91]. The fact that this acid has long carbon chains; it is able to form few monolayers on top of the nanorods. These

layers have wax like properties, which transfer the surface energy from highly surface tension to low surface tension. It is important in mind that this method of getting superhydrophobic surface requires to have high surface roughness first. In the scope of this dissertation the surface roughness was obtained through the ZnO nanostructures grown on the solar cell surface.

The procedure in which the ZnO nanostructures treated for hydrophobicity is done by immersing the solar cell with the ZnO nanoneedles on top of it in a 20 mM Stearic Acid solution in Ethanol. The sample kept in this solution for 24 hours, followed by annealing in closed furnace at 100 ^{o}C for three hours. The sample then left in open air in a dust free environment for another 24 hours. After the last step the surface has shown superhydrophobic properties by repelling water droplets directed to it.

III. Device and Materials Characterization Techniques

Several characterization techniques were used throughout the course of this project. These techniques were used to characterize both the device performance and the grown materials quality and properties.

A. Device Characterization Techniques

Current-Voltage Characteristics

The Current-Voltage (IV) measurements can be considered one of the most important measurements that can present the device performance. Important factors such as power conversion efficiency, filling factor, open circuit voltage and short circuit current can be extracted from this measurement. The IV characteristics of the fabricated solar cells were obtained by using Keithley SCS 4200 characterizer in conjunction with AM1.5 solar simulator. This characterization system consists of a source measuring unit that can bias the solar cell and measure simultaneously. The bias is done through a voltage sweep between two limits that user can define, and depends on the solar cell bandgap. While sweeping voltage the system is capable of measuring the solar cell current. The used systems is shown in figure 3.1 (a), and figure 3.1 (b) shows the gold wire bonder that is used to wire the solar cells on device holders. The solar cells were characterized between -1.2 V – 1.2 V limits, which is higher than the highest value of open circuit voltage (~ 1V) obtained for the reference solar cell.

(a) 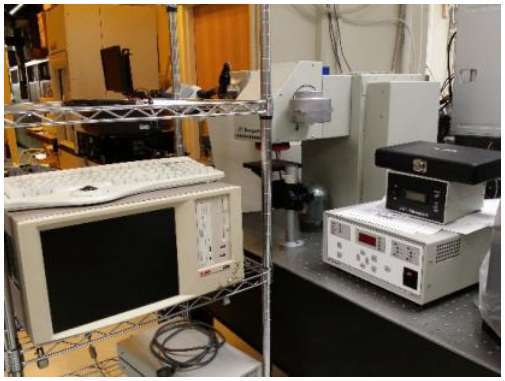 (b) 

Figure 3.1. (a) Keithley SCS 4200 characterizer and the 1.5M solar simulator. (b) Gold wire bonder. "Photo by Yahia Makableh"

Spectral Response Characterization

The spectral response of a solar cell can be explained as the response of a solar cell to an absorbed photon at a certain wavelength and the ability to generate an electron due to photon absorption. Hence, the spectral response is related to the short circuit current generated with respect to the input power from the incident photon. Since the solar cell cannot absorb any photons below its bandgap, the spectral response of any solar cell will drop to zero at that point. In this project, Bruker 125HR FTIR spectrometer, integrated with a Keithley 428 current preamplifier was used. This system is capable of measuring absorption and emission spectra.

In general, the system has a Michelson Interferometer, a wide range light sources and a light detector. The used Interferometer has a beam splitter, with two mirrors one fixed and one can move. When the movable mirrors change position the output of the system change with it, which is transferred into a spatial coordinate by using signal Fourier transform. The change in position of the movable mirror is detected by using a HeNe laser. The light is generated by a quartz halogen source and a quartz beam splitter with range of the quartz halogen source between ranges: 5000 cm^{-1} – 25000 cm^{-1}. Due to the presence of the beam splitter, no response can be obtained bellow 500 nm range. A Janis Cryostat was used to hold the solar cells, and the

system chamber pressure was held at ~10^{-5} Torr range. The measurements were performed at room temperature. The Bruker 125H system is shown in figure 3.2.

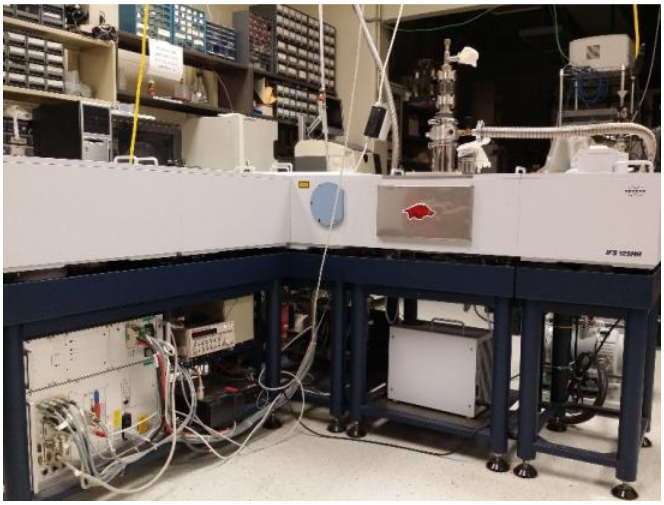

Figure 3.2. Bruker 125HR FTIR spectrometer. “Photo by Yahia Makableh”

Quantum Efficiency

The quantum efficiency of a solar cell can explained as the ratio between the number of generated electrons per the number of incident photons at certain wavelengths. The quantum efficiency of an ideal solar cell should be 100 %, assuming that any incident photon will be able to generate one electron. In fact, the ideal case cannot be achieved due to many factors involved in the light-matter interactions. Some of these factors are low diffusion lengths, and front and back surface recombination. Furthermore, the quantum efficiency of any solar cell will drop to zero bellow the bandgap, as there will be no more photons able to generate any electrons after this point. There are two types of quantum efficiency, external and internal quantum efficiencies. The difference between both is that external quantum efficiency takes into place optical losses surface reflection, while internal quantum efficiency is only ratio measure between incident photons and generated electrons. Throughout this project the focus was on external quantum efficiency (EQE).

The system used to record the external quantum efficiency spectra of the solar cells is Newport IQE 200. The system contains white light sources, passes through 30 Hz frequency chopper then a monochromator. The system is equipped with a lock-in amplifier that only allows the detection of signals at 30 Hz, in order to eliminate white light noise from outside sources. Then a beam splitter split the light into two parts, the first part goes to a reference detector and the other part goes normal to the solar cell surface. A second detector aligned to the solar cell direction is used to detect the reflected light from the solar cell. From all these parts the system can calculate the value of the external quantum efficiency as:

$$QE(\lambda) = \frac{hcS(\lambda)}{\lambda q} \tag{3-1}$$

where $S(\lambda)$ is the power spectral responsivity (nm/A). The Newport IQE 200 device is shown in figure 3.3.

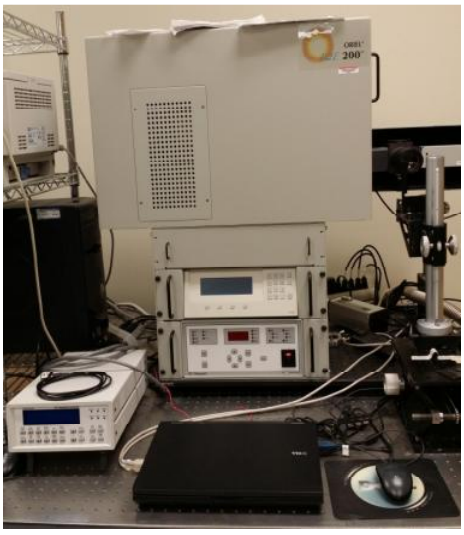

Figure 3.3. Newport IQE 200 quantum efficiency system. “Photo by Yahia Makableh”

B. Materials Characterization Techniques

Ultraviolet-Visible-Near Infrared Spectroscopy

Through the process of growing the different anti-reflection coating compounds, and applying them to devices two measurements were used. These two measurements are absorption and transmission spectra. Both were done between 200 – 1600 nm. In the absorption spectra the focus was on the liquid materials in order to check for any absorption peak that is linked to the grown material bandgap. This test is very important in order to have first identification of the material, and second to have a proof that the grown compound is what it should be. For example, the bandgap of ZnO is around 3.3 eV, which can give an absorption peak around 375 nm. Therefore, if the synthesized ZnO sol-gel did not have an absorption peak at 375 nm, then the compound did not transformed to ZnO and cannot be used in any further steps. On the other hand, the transmission spectra were usually obtained for semi-insulating GaAs samples coated with the anti-reflection coating material. This measurement gives information about the enhancement in transmission (reflection reduction) after coating the GaAs with any ARC material. Also, it is used to optimize for the spin coating speed of the ARC on GaAs in order to get the speed that gives the highest possible transmission.

These two tests were done by using Carry500 UV-Vis-Nir spectrometer. In this system a wide range light source is used. Light sources generates light that passes through the sample under investigation, then the light will encounter one of three possibilities: Reflection from the surface, absorption in the material or transmission through the sample. In Carry500 the incident light intensity I_o, and the transmitted light intensity I are detected by two different detectors, which can generate absorbance of the sample with respect to the generated light. The absorbance

A can be defined as the measure of light loss due to light scattering and light absorption when passes through a medium, and can be explained in the flowing equation:

$$A = -\log T = -\log \frac{I}{I_o} \tag{3-2}$$

where *T* is the intensity of the transmitted light. The Carry500 system is shown in figure 3.4.

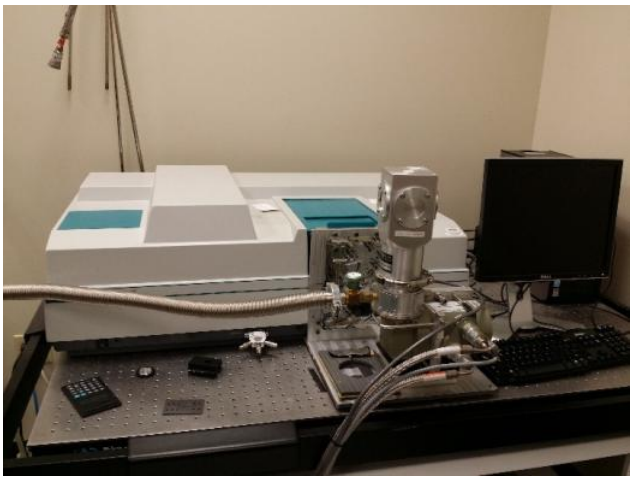

Figure 3.4. Carry500 UV-Vis-Nir spectrometer. "Photo by Yahia Makableh"

Raman spectroscopy

The second type of measurements that was used to identify the material formation and quality is Raman spectroscopy. LabRam HR from Horiba equipped with 472 nm blue laser was used in this project. Raman can be explained as the observation of the material atoms vibrational modes. The atoms vibration is different from material to material, so each material can give different Raman spectra than other materials. Raman spectra give a fingerprint about each material; from which the new grown material spectra can be compared with theoretical or published data for comparison. For the purpose of this project Raman spectra were obtained by using Micro Raman for the coated samples with ARC materials. Since these ARC layers are less

than 100 nm in depth, or contains nanostructures, Micro Raman served as a better Raman system over regular Raman due to the fact the laser beam can be focused in small area that can detect vibrations from nanostructures. A picture showing the Micro Raman system is presented in figure 3.5.

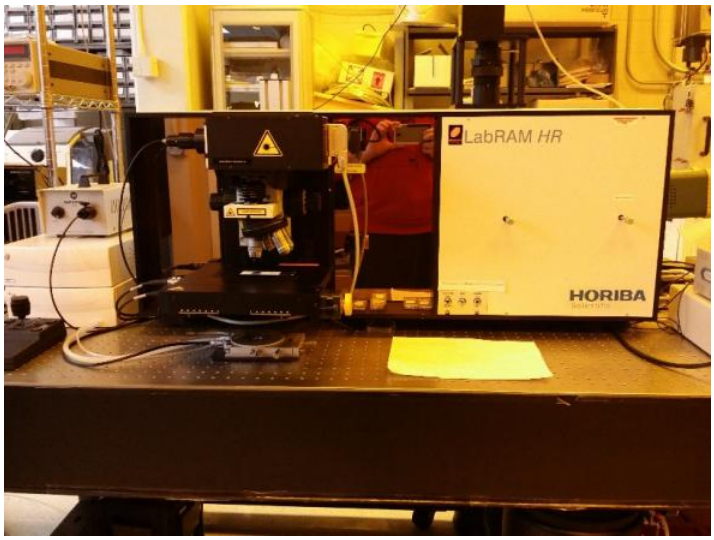

Figure 3.5. HORIBA LabRam HR Micro Raman system. “Photo by Yahia Makableh”

Ellipsometry Spectroscopy

Ellipsometry spectroscopy is a measurement can be performed on optical coatings and thin films to obtain different optical properties of the materials. From this measurement the refractive index, thickness, surface roughness, and light reflection can be obtained. In this measurement the dielectric function of the material can be found by using polarized light, which can be used to obtain the other optical properties mentioned through different mathematical models for the different materials. In this study a J. A Woolam VASE ellipsometer was used.

X-ray Diffraction

The fourth materials characterization method used was X-ray diffraction. This method is usually used as a nondestructive method to give materials signature such as Lattice spacing, crystal orientation and structure. In X-ray diffraction measurement a high energy X-ray beam incident to the crystal scatters elastically from the different crystal plans (Thompson scattering). Therefore, the atoms will vibrate at frequency equals the X-ray frequency. Interference can occur at the different scattered plans, which can be detected and recorded as shift from the original incident wave, called diffraction pattern. The measured diffraction patterns can then be analyzed to give certain materials characteristics such as the crystalline structure. As in Raman, each different material will give different diffraction pattern that is unique signature for that specific material crystalline structure. The ARC materials were measured by using Philips PW 3040 X'PERT MRD high resolution XRD machine.

Surface Morphology Microscopy

In order to obtain more information about how the surface of the ARC films looks like, Scanning Electron Microscope (SEM) and the Atomic Force Microscope (AFM) are used. The SEM system used is a FEI xT Nova NanoLab 200 and the AFM system is Veeco Dimension 3100. In SEM system a focused ion beam is focused by using an electromagnetic field towards the surface of the sample under investigation. After the accelerated electrons hit the surface some of them will be diffused into the material while other interact with the material atomic electronic structure which them forms secondary electrons that are reflected from the surface. These reflected secondary electrons then are detected and used to generate images showing the

sample morphology. The SEM is used to test larger areas than AFM, in a faster manner with high resolution.

Some nanostructures that can suffer from electrons charging effect on the surface, that cannot be measured using SEM, are measured with AFM. The AFM is also used in high resolution nanoscale topography imaging. Not like SEM which uses an electron beam, AFM uses a probe that can come into contact with the surface to redraw the surface profile. This can be done with the optical system the AFM equipped machine. Usually the probe is a cantilever beam that oscillates and can come in contact with the surface. A laser beam is directed towards the back side of the cantilever beam, and a 4-segmnet position sensitive photodiode is used to detect the reflection of the laser from the cantilever beam. Different laser reflection will correspond to different detection areas on the 4-segment photodiode. By using this mechanism the AFM machine can obtain the surface morphology and display it on a screen.

Both SEM and AFM tools can be used alternatively and depends on the sample under investigation. Usually SEM requires ultra-high vacuum compared with no vacuum requirements for AFM. Also SEM can be faster way of measurement and can cover larger areas compared with AFM, but SEM cannot be used with nonconductive samples that allows electron accumulation on the surface which leads to no SEM beam stability then losing the image quality.

IV. Solar Cell Devices Characteristics

A. Introduction

Intermediate band solar cells have gained giant research attention lately. This is due to their ability to generate higher short circuit currents, and their extended response beyond the host material bandgap. The focus in this project is on InAs quantum dots solar cells embedded in $In_xGa_{1-x}As$ quantum wells with GaAs as host materials, where x represents the In mole fraction and was varied between 0 – 25 %. The presence of the InAs quantum structures allows bandgap tuning between the GaAs and InAs bandgaps, respectively. Also the spectral response of the solar cells was extended to the near infrared region.

B. Solar Cells Device Structure

The solar cells structures were grown with MBE method. The host material is GaAs. In these solar cells, ten periods of InAs quantum dots (each is 2ML) were grown with 5nm $In_xGa_{1-x}As$ quantum well and 35 nm GaAs barrier, grown on an n-type GaAs substrate, with an n-type buffer layer on top of it doped with [Si] = 5 x 10^{18} cm^{-3}. A back surface field layer was embedded in the buffer layer as a 100 nm thick layer doped with [Si] = 1 x 10^{18} cm^{-3}. The quantum dots were doped with [Si] = 2x10^{17} cm^{-3}. The n-type doping of the quantum dots enabled the quantum dots to have partially filled intermediate bands, which makes allows the transition of carriers through the intermediate bands. The quantum structure was grown within the depletion region of the GaAs pn junction. A p-type layer doped with [Be] = 1 x 10^{18} cm^{-3} was used to cap the quantum structure. A window layers was embedded in the cap layer as 40 nm thick layer doped with [Be] = 1 x 10^{18} cm^{-3}. The purpose of the window layer is to reduce the surface recombination by passivating the p-type GaAs surface states. Similar to this

function, the n-type back surface field layer also passivates the junction interconnects to reduce the back surface recombination,

C. Results and Discussions

Different structures with different In mole fraction (x) were grown. The groan wafers had In mole fractions as the following: 0 %, 10 %, 15 %, and 25 %. Additionally, a pn junction GaAs reference cell was also grown in the same manner discussed before, but without having any quantum structures in the depletion region. Solar cells were fabricated from each wafer following the procedure discussed in chapter 2. After fabrication each solar cell was then characterized using IV measurements, external quantum efficiency (EQE), and spectral response measurements. All device characterizations were done at room temperature.

Current Voltage Measurements

The IV characteristics were obtained for the different solar cells under illumination of 1-3 suns. The IV for all the solar in comparison with pn junction GaAs solar cells are plotted in Figure 4.2. It has been seen from the IV of the quantum dots solar cells that the short circuit current was increased compared with the reference cell. This increase in the short circuit current is attributed to the interband transitions in the quantum dots. Also, the carrier tunneling between the intermediate band can contribute to the increased short circuit current. This effect is consistent with other reported results by other published results [92]. On the other side, the open circuit voltage was dropped in all quantum dots devices, leading to decreased device power conversion efficiency. The decreased open circuit voltage is expected due to the bandgap of the solar cell was decreased with increasing the In mole fraction in the different solar cells. Additionally, the lattice mismatch between the GaAs and InAs can generate charge traps that

could also affect the open circuit voltage. One of other reasons behind the degradation in the open circuit voltage is also the recombination that can occur inside the quantum dots as well [1]. All these factors mentioned made the open circuit voltage in the InAs quantum dots solar cells to have lower power conversion efficiency compared to the reference solar cell. The IV characteristics of the different InAs quantum dots with comparison to the pn junction cell are shown in figure 4.1 [1].

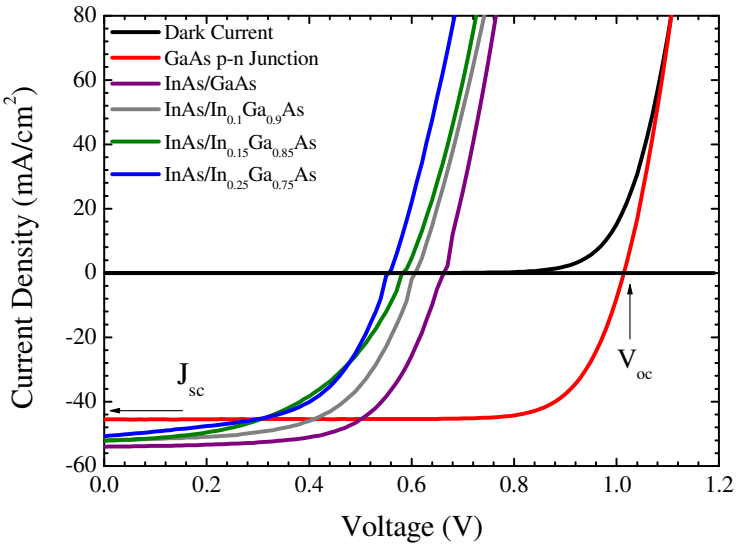

Figure 4.1. Current-voltage characteristics of InAs quantum dots solar cells with comparison to GaAs reference cell, measured at room temperature. Reprinted with permission from Vasan *et al* [21].

External Quantum Efficiency Measurements

The external quantum efficiency is an important measure of the device spectral range, and also strongly related to the power conversion efficiency. As mentioned before, EQE is a measure of the ratio between the excited electrons per incident photon. The EQE spectra of the different solar cells plotted with comparison to the reference cell are shown in figure 4.2 [1]. From the spectra of the different solar cells, it has been noticed that InAs quantum dots solar cell

has improved spectra below the 700 nm range, and also has extended response beyond the GaAs cutoff point. This enhancement can be related to the transitions from the bound states to the continuum levels in the quantum dots. On other side, the response beyond the GaAs cutoff point is related to the interband transitions in the quantum dots, which is strong evidence of their effect on the device performance. Beside the main peaks that are seen from the interband transitions, there are several smaller peaks can be mentioned also. These lower response peaks are due to the intersubband transitions. Since the response from these transitions are very low they are not expected to contribute to the photocurrent generation.

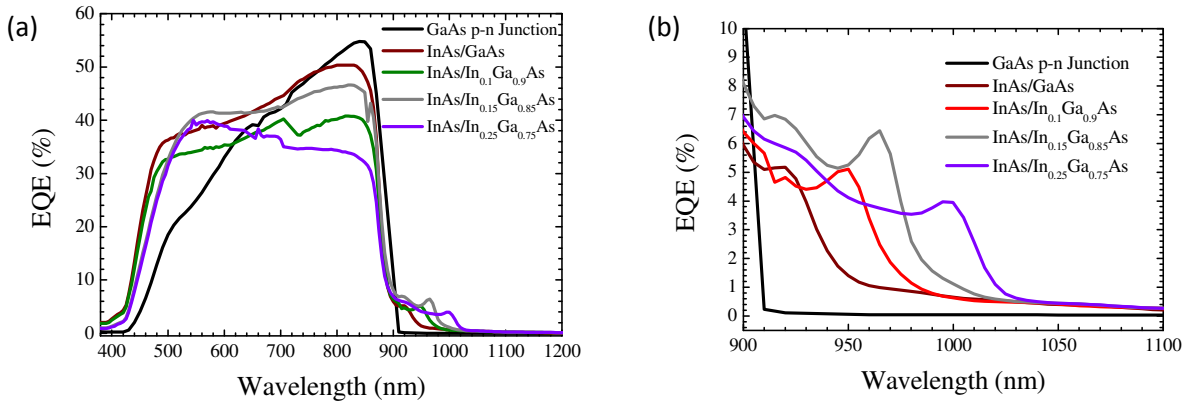

Figure 4.2. (a) External Quantum Efficiency spectra of InAs quantum dots solar cells with comparison to GaAs reference cell, measured at room temperature [1]. (b) The response from the InAs quantum dots beyond the GaAs bandgap limit. Reprinted with permission from Vasan *et al*

Spectral Response Measurements

To further investigate the effect of introducing the quantum dots on the solar cells, spectral response measurements can be performed. This measurement has been done using FTIR Bruker 125H system. The spectral response measurements were also performed at room temperature and shown in figure 4.3 [1]. The rapid decay in the response bellow 700 nm range is

due to the beam splitter that is used in the Bruker system. Additionally, the quantum dots response has a remarkable improvement on the solar cell response bellow the GaAs bandgap. From the spectra also the intersubband transitions are more clear in this measurement

The results obtained from both the external quantum efficiency and the spectral responses are both in agreement with each other. Both measurements show the extended response of the quantum dots solar cell compared with the reference cell. Moreover, both measurements show the interband transitions from the quantum dots. These transitions are directly related to the enhanced photocurrent generation mentioned in the IV characteristics of the solar cells. Hence all three measurements are consistent and validate the ability of the quantum dots to play a major rule in the solar cells performance.

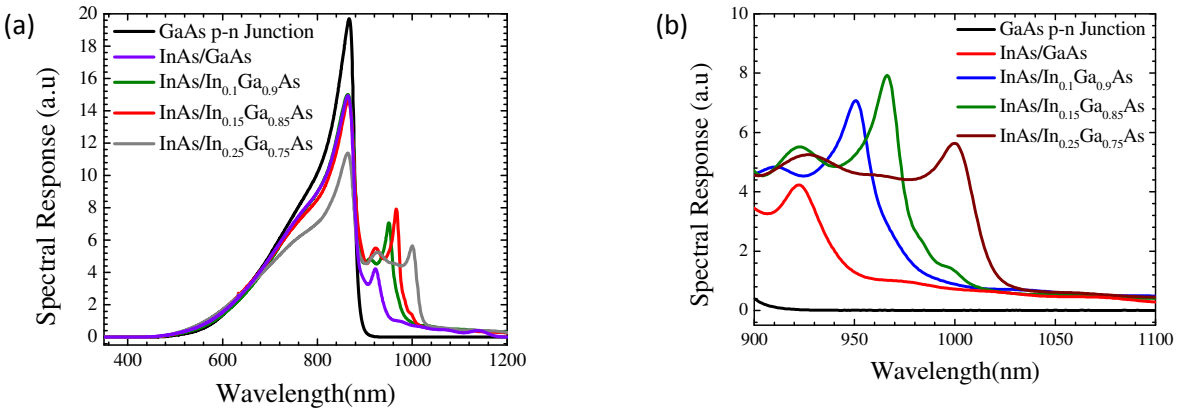

Figure 4.3. (a) Spectral response spectra of InAs quantum dots cells compared with GaAs pn junction reference cell measured at room temperature [1]. (b) The response of the InAs quantum dots beyond the GaAs limit. Reprinted with permission from Vasan *et al*

V. Plasmonic Effect on Solar Cells Performance

A. Introduction

The metal nanoparticles were grown by using chemical colloidal method and e-beam deposition. The nanoparticles absorption spectra were obtained by using Cary500 spectrometer. Scanning electron microscopy was used to find the metal nanoparticles size and distribution. The nanoparticles were then applied to solar cell devices, and their effect on the cells performance was characterized by IV, EQE and spectral response measurements.

B. Metal Nanoparticles Characteristics

Colloidal Metal Nanoparticles

After the nanoparticles synthesis using colloidal growth method, the absorption spectra were obtained for both the Ag and Au nanoparticles. The absorption spectra of Ag and Au nanoparticles are shown in figure 5.1.

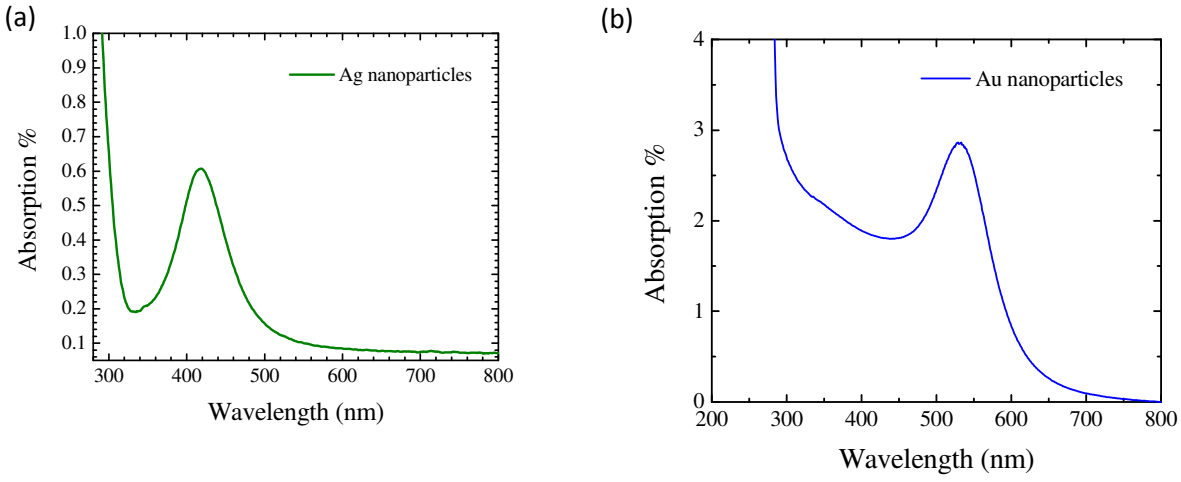

Figure 5.1. Absorption spectra of (a) Silver nanoparticles, and (b) Gold nanoparticles

From the absorption spectra Ag has an absorption peak (~ 420 nm), and Au has absorption peak (~ 530 nm). Both peaks are consistent with published results for colloidal Ag and Au [79], [80]. The stronger percentage absorption seen with Au nanoparticles compared to the Ag nanoparticles is related to the nanoparticles concentration in Toluene. Since the response from both types of nanoparticles overlaps the GaAs spectral response, then the plasmonic effect that can present will change the solar device performance. The nanoparticles were then deposited on GaAs substrates. For this purpose Poly-L-Lysine (PLL) polymer linkers were used to attach the nanoparticles to the substrates surfaces [93]. Both the size and distribution of the deposited nanoparticles were found by using SEM, and shown in figure 5.2.

The average size for both Ag and Au nanoparticles is 10 nm and 20 nm, respectively. It is clear from the SEM images how the Au nanoparticles have higher concentration on the surface compared with the Ag nanoparticles, which is consistent with the amplitude of the absorption spectra as mentioned before. Additionally, the Au nanoparticles show larger sizes than Ag nanoparticles, this consistent with the absorption peaks for both Au and Ag that confirms Au should have larger size than Ag nanoparticles. This is clear from the red shift of the Au nanoparticles absorption compared to Ag nanoparticles absorption. The effect of coupling these nanoparticles to real devices is discussed in later sections.

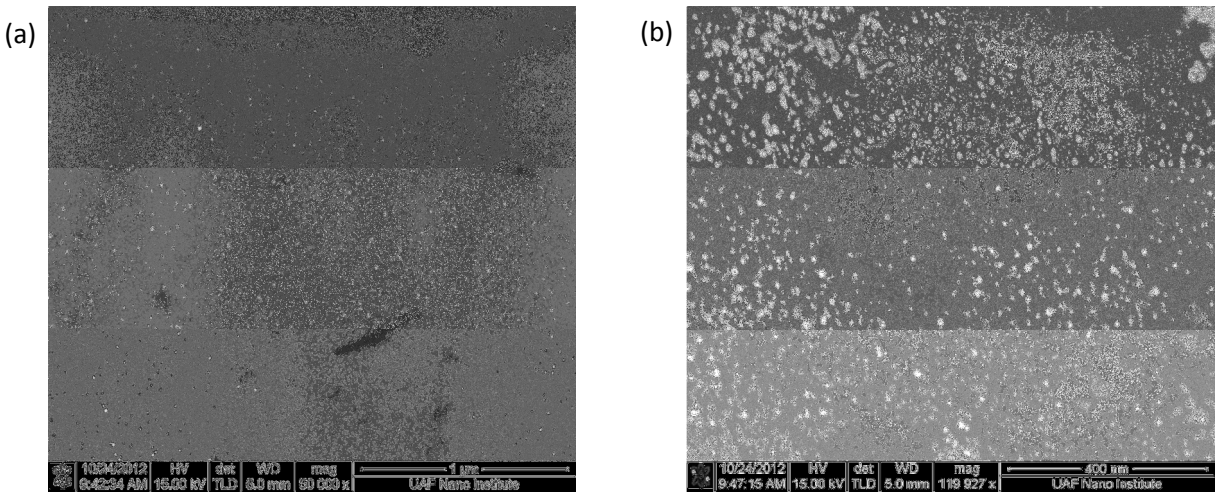

Figure 5.2. Scanning electron microscopy of (a) Silver nanoparticles coupled to GaAs surface, and (b) Gold nanoparticles coupled to GaAs surface.

Electron Beam Deposited Nanoparticles

Electron beam deposition of metallic nanoparticles has great potential in the plasmonic effect field. The easier use of e-beam for nanoparticles deposition compared with the cost and time associated with the colloidal growth may rise the importance of using this tool for advance research. The formation of metallic nanoparticles by using e-beam deposition can occur by evaporating the needed materials at a very low rate, high vacuum and small thicknesses. For example Ag nanoparticles can form on any type of substrate without using any linkers by e-beam deposition if the thickness deposited was less than 2 nm at rate of 0.25 A^{o}/second. This small thickness and slow rate promotes the formation of well distributed nanoparticles all over the substrate surface. In this study, both Au and Ag nanoparticles were deposited by using e-beam deposition with thicknesses of less 0.5 nm – 1 nm and deposition rate of 0.25 A^{o}/second. Both glass and GaAs substrates were used in this experiment. The glass substrate was used in order to evaluate the absorption spectra of the deposited nanoparticles. Also, SEM was used to obtain the

surface morphology of the deposited nanoparticles were both the size and surface filling can be known from it.

The absorption spectra of the deposited nanoparticles on glass are shown in figure 5.3. Both graphs were obtained after depositing 1 nm and 2 nm of the metal nanoparticles. During the deposition the substrate was held at 100 ^{o}C, this allows annealing in vacuum while deposition, which helps in the nanoparticles formation process. Both spectra reveal how the deposited thickness plays a role in changing the absorption intensity. The higher deposited thickness is the higher absorption. On the other hand, there is small red shift in the peak with higher deposited thickness; this is related to the bigger nanoparticles size which has direct relationship with the deposited thickness. Moreover, the absorption peaks for both Ag and gold by using e-beam deposition are consistent with the absorption peaks found for the colloidal grown nanoparticles.

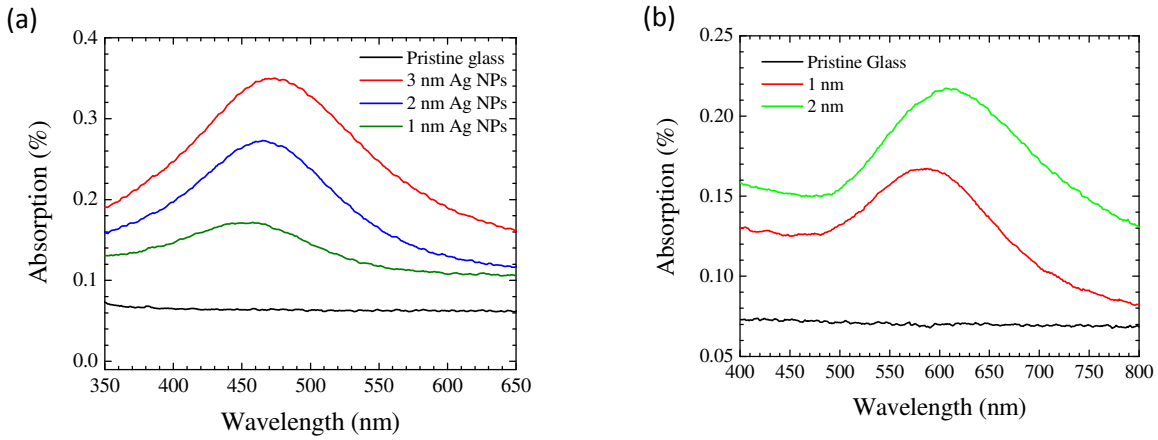

Figure 5.3. Absorption spectra of e-beam deposited nanoparticles (a) Silver nanoparticles on glass, and (b) Gold nanoparticles on glass.

For further investigate the e-beam deposited nanoparticles, the absorption spectra of Au nanoparticles were obtained for another set of samples before and after annealing. The annealing was carried out in tabular furnace, at a temperature of 250 ^{o}C under nitrogen flow. Figure 5.4 shows the nanoparticles absorption spectra before and after annealing. The annealing of the nanoparticles at high temperature has an effect as the absorption intensity decreases after annealing. The change in the intensity and the peak position can be related to the nanoparticles size change, as annealing could lead to aggregation, which lowers the quality of the as deposited nanoparticles.

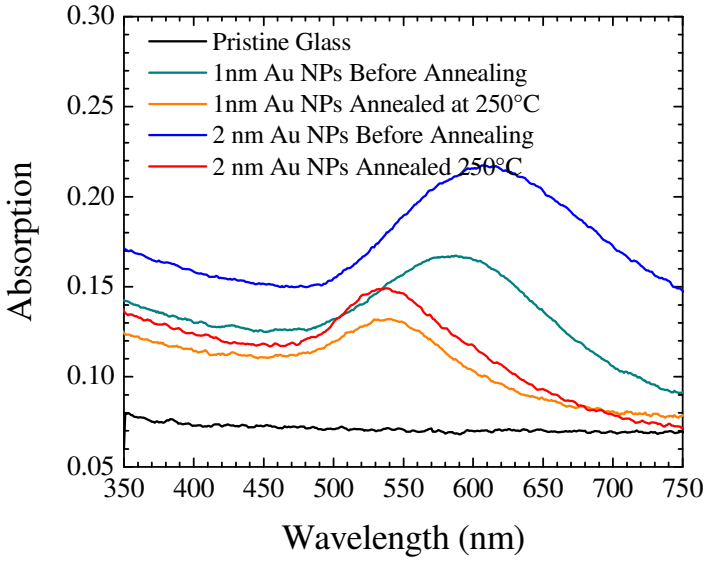

Figure 5.4. Absorption spectra of Au nanoparticles deposited using e-beam before and after annealing at high temperature.

The deposited nanoparticles size and distribution were images with SEM. For this purpose the substrate used was GaAs to eliminate the charging effect that form on glass surface. Also this will be the real case when coupling the nanoparticles to the solar cells. The SEM images are shown in figure 5.5.

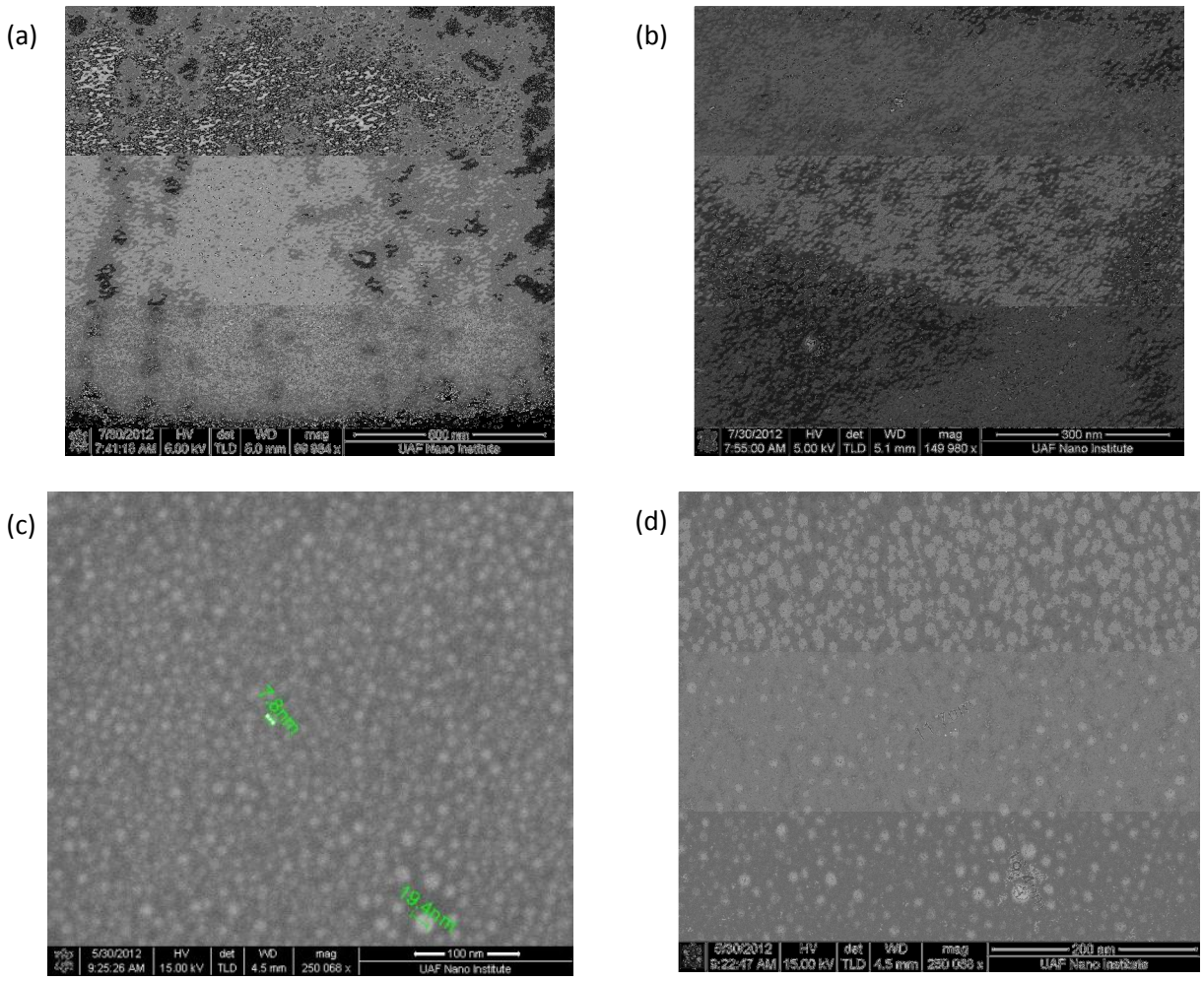

Figure 5.5. Scanning electron microscopy images of e-beam deposited nanoparticles on GaAs (a) Silver nanoparticles at 500 nm scale, (b) Silver nanoparticles at 300 nm scale (c) Gold nanoparticles at 100 nm scale and (d) gold nanoparticles at 200 nm scale

From the SEM images the nanoparticles have a size range between 7 nm – 20 nm for the Au nanoparticles, and between 5 nm – 15 nm for the Ag the nanoparticles. Additionally, the surface coverage for both nanoparticles is high in both types. After the metallic nanoparticles characterization and deposition process optimization was completed, they were applied to InAs quantum dots solar cells to see how they affect the device performance.

C. Plasmonic Nanoparticles Effect on Solar Cells

The grown metal nanoparticles were tested on InAs quantum dots and reference cell devices. The colloidal nanoparticles were linked to the surface of the cells by using Poly-L-Lysin. Before linking the nanoparticles to the solar cells a pre-cleaning process was followed. The cleaning process can be described as follows: First the cells were cleaned with organic solvents. Acetone, Methanol and Isopropanol were the solvents used. Between each solvent the cells were washed with DI water and blown dry with nitrogen gas. The cells were immersed in each solvent for three minutes. Second the solar cells were cleaned with 6 % HCL to remove any oxide layers from the cells surfaces. After cleaning with HCL the cells were ready for nanoparticles linking.

The linking process is also divided into two parts, the first part is to attach the PLL linkers to the solar cell surface. This was completed by immersing the samples in a 1 to 1 PLL:H_2O solution. The immersion time was five hours. This time allow the surface to have enough linkers that can attract the metal nanoparticles to it. After immersion is completed, the cells were then cleaned with DI water to remove any excess linkers from the surface. Followed by immersing the cells in the nanoparticles solution. The cell immersion in nanoparticles solution was optimized to be 30 minutes. The cells were then taken of the nanoparticles solutions, and rinsed with Ethanol to remove excess formation of nanoparticles on the surface. Post-annealing was performed in tabular furnace at 200 ^{o}C under nitrogen flow. The annealing can ensure evaporation of any organic solvents or materials from the cells surface, which can affect the cells performances. Device characterization was then carried out.

Solar Cells Performance with Colloidal Nanoparticles

In this measurement InAs/$In_xGa_{1-x}As$ quantum dots, with x = 10 % Indium were used. The device characterization after linking the colloidal nanoparticles was carried out by IV, EQE and spectral response measurements. The measurements were done at room temperature before and after linking the nanoparticles to them. The IV characteristics for a solar cell linked with Ag nanoparticles, and a solar cell linked with Au nanoparticles are shown in figure 5.6. It is noticed that both solar cell has better power conversion efficiency compared with the pristine case. The cell with Ag nanoparticles had a 17 % improvement after coupling it with Ag nanoparticles. On the other hand the cell with Au nanoparticles had only 5 % of power conversion efficiency enhancement. The better enhancement seen with the Ag nanoparticles is related to different reasons. The first reason it is that Ag has higher electrons density, which makes it a better material for Plasmonic effect material. Second the Au nanoparticles have more size and more density on the surface, which could produce a shadow effect on the solar cell.

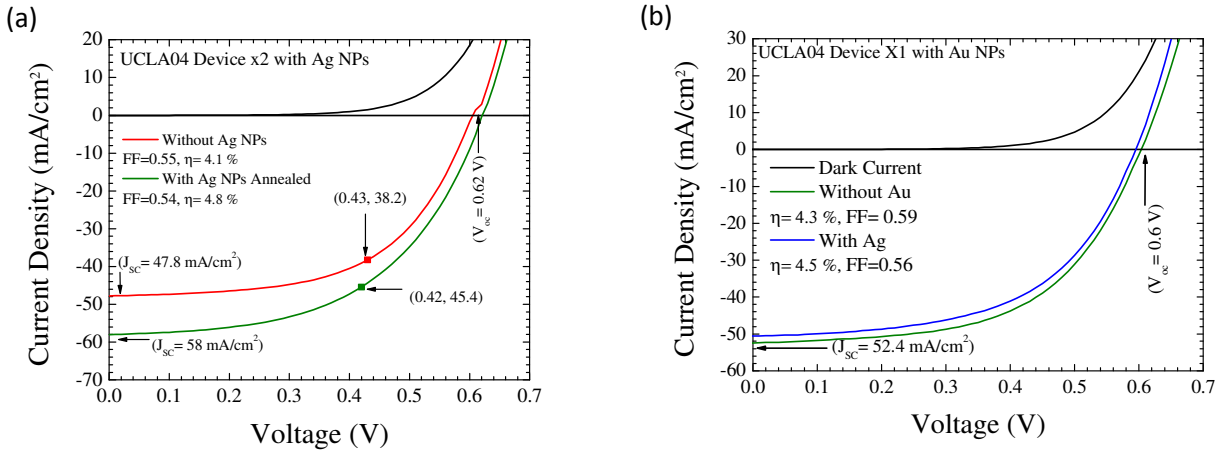

Figure 5.6. Current Voltage characteristics of InAs quantum dots solar cells before and after coupling the cells with (a) Colloidal Ag nanoparticles, (b) Colloidal Au nanoparticles

Similar enhancement was noticed in both the external quantum efficiency and the spectra response measurements. The EQE and the spectral response spectra are shown in figure 5.7 for the device before and after coupling them with metallic nanoparticles. The enhancement due to Ag nanoparticles was higher than the enhancement seen after using Au nanoparticles with these InAs quantum dots solar cells. These results are in agreement with the IV characteristics as mentioned earlier. The response from the quantum dots is visible in both cells, but no significant enhancement in their response after coupling the solar cells with the metallic nanoparticles.

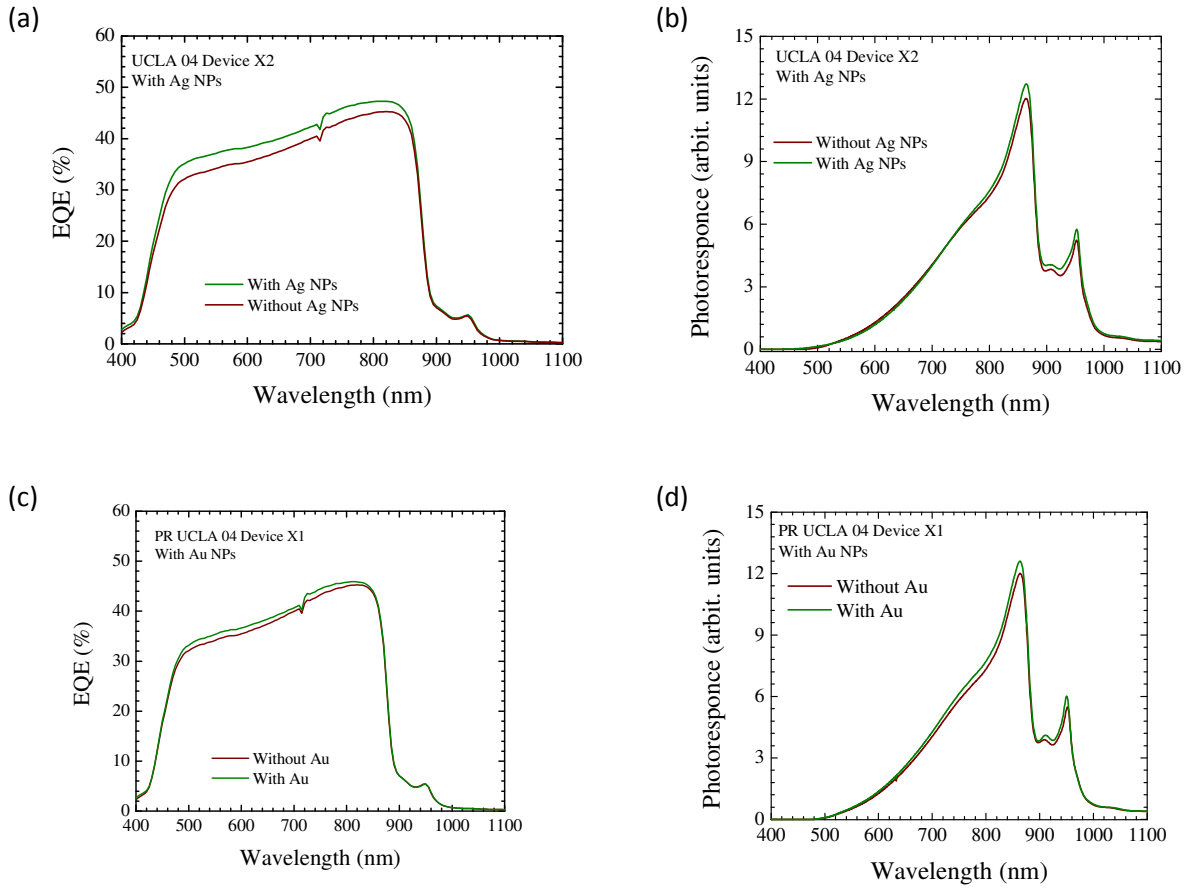

Figure 5.7. External quantum efficiency and spectra response spectra of InAs quantum dots cells before and after coupling them with (a, b) Ag nanoparticles, (c, d) Au nanoparticles

Solar Cells Performance with E-beam Deposited Nanoparticles

The size formed with the e-beam deposited nanoparticles was consistent with the colloidal grown nanoparticles. Despite the same size their density on the surface was much higher than the colloidal growth nanoparticles. These properties gave noticeable absorption spectra that were in the same order as the chemically grown nanoparticles as well. To study their effect on the InAs quantum dots solar cells both Ag and Au nanoparticles were deposited on real device. The deposited thickness was 1 nm, while keeping the substrate temperature at 100 ^{o}C. High vacuum was maintained at around 5 x 10^{-7} torr during the deposition process, and 0.25 A^{o}/second was the evaporation rate. The IV characteristics of both cells used in this experiment are shown in figure 5.8. The devices did not face any enhancement after depositing the metallic nanoparticles on them. This is related to high density of the deposited nanoparticles compared with the colloidal nanoparticles. Other attempts were taken to reduce the nanoparticles density b depositing less thickness down to 0.5 nm but the same problem remained. Hence no further investigation was carried out for these devices.

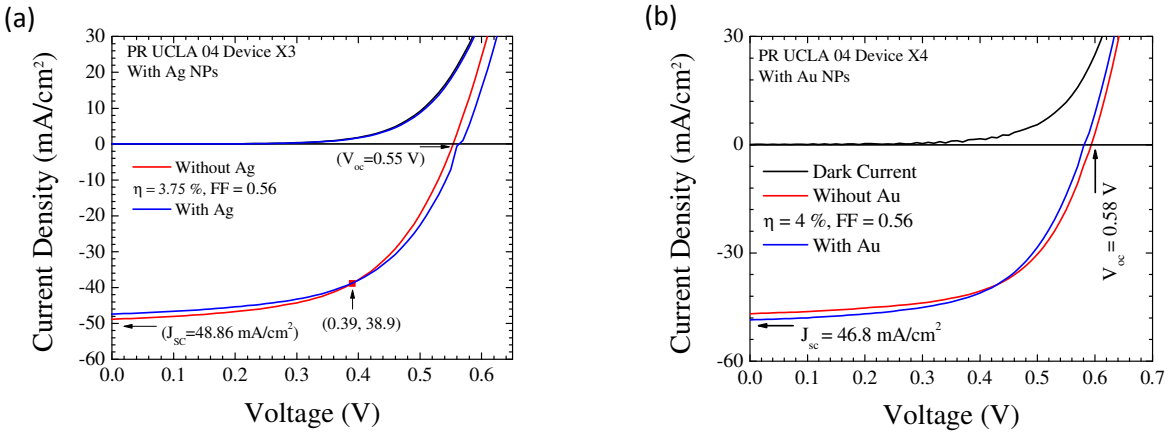

Figure 5.8. The IV characteristics of InAs quantum dots solar cells with e-beam deposited nanoparticles (a) Ag nanoparticles, (b) Au nanoparticles

VI. Device Performance Enhancement by using Anti-Reflection Coatings

A. Introduction

Several materials have been used as anti-reflection coatings in general. The focus in this project is on oxide and florid materials where they can be grown either by sol-gel method or by e-beam deposition. The materials that were synthesized by using sol-gel method are ZnO, TiO_2, SiO_2, and ZnS. On the other side, e-beam deposition was used to deposit MgF_2 on the solar cells. Beside the process of forming layered films on top of the solar cell, ZnO nanoneedles and SiO_2 nanoparticles were used also to investigate their effect on the device performance, and also to be used in the superhydrophobicity treatment. The grown materials and the deposited layers were characterized by using UV-Vis-NIR, Raman, and XRD spectroscopies. The optical properties and reflection spectra were obtained by using Ellipsometry measurements.

B. Materials Deposition, Characterization and Optimization Process

The selection of materials used in this project is due to their low cost, nontoxicity, and simplicity of growth process compared to other materials. Additionally, these materials have refractive indices that match the best ARC for GaAs according to equation 1-5. All of ZnO, TiO_2 and ZnS have refractive indices (~2), while SiO_2 and MgF_2 have refractive indices closer to (~1.4). Therefore, the first set of high refractive indices materials can be used a single layer coatings, or as first layer in a two layered ARC. For the sol-gel synthesize compounds spin coating was used to coat the cells with these materials. Absorption spectra of ZnO sol-gel measured at room temperature is shown in figure 6.1 (a).

To optimize the process for each material, first the materials were spin coated on semi insulating GaAs at different speeds, and times. These speeds were ranging between 4000 rpm – 12000 rpm. The times were varied between 30 seconds to 60 seconds. After this process the

coated samples were then annealed in tabular furnace under vacuum at temperatures below 300 ^{o}C. This higher limit temperature was defined by testing pn junction GaAs solar cell and quantum dots solar cells at different temperatures to know where the pn junction will break and hence the whole cell device is not functional.

From experimental results the highest safe temperature for these solar cells found to be 300 ^{o}C. The ARC annealing process is important in order to take out all the organic compounds and also to make the film more uniform all over the surface. Also, annealing can improve the deposited layers quality by making the material more crystalline than amorphous material. After annealing the coated samples then they were measured with Carry500 to obtain the transmission spectra between 800 nm -1600 nm. This range is the closest range to the solar cell spectral response. No transmission spectra can be obtained to GaAs below 800 nm as the bandgap of GaAs limits transmission bellow this point. The change of GaAs surface color after depositing ZnO on top of it at different speeds is shown in figure 6.1 (b), where the samples starting from top right corner are GaAs coated at: 4000 rpm, 6000 rpm, 8000 rpm, 10000 rpm, 12000 rpm, and pristine GaAs. It is very clear how the color of GaAs changed from dark gray to blue color after coating with ZnO. The color change is due to the light interference with the ZnO deposited layers.

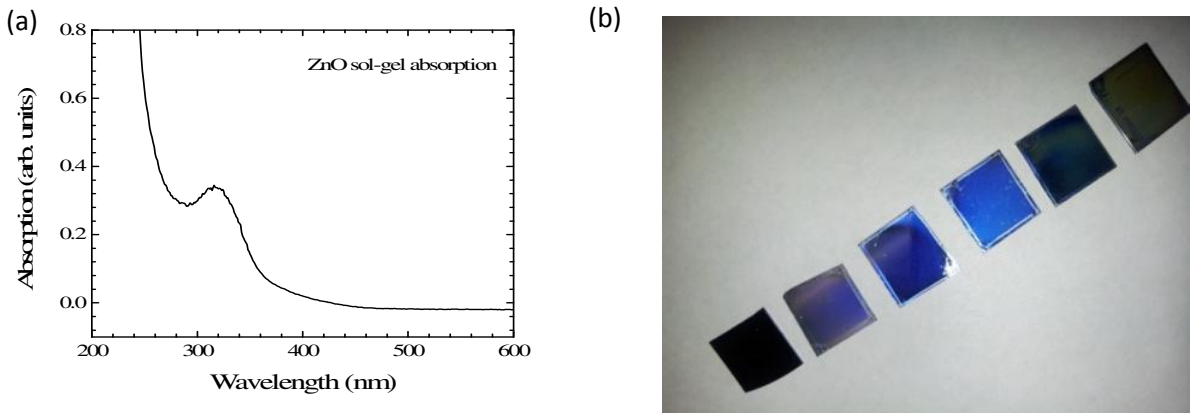

Figure 6.1. (a) Absorption spectra of ZnO measured using Cary500. (b) Surface color change of semi-insulating GaAs after coating with ZnO at different spin coating speeds. "Photo by Yahia Makableh".

Anti-Reflection Coating Transmission Measurements

The transmission spectra of the different ARC materials used in this project were obtained in order to optimize the spin coating process. The thickness of the spin coated layers changes with changing the speed, so the transmission spectra can change as well. For each material different semi insulating samples were spin coated with that material sol-gel at different speeds. Figure 6.2 shows the transmission spectra of different materials spin coated on GaAs. From the figure it is clearly visible how the spin speed can change the transmission of GaAs. Also, it can be noticed how each material can give different spectra compared to other materials at the same spin coating speed. These differences are related to compounds viscosity, sticking ability on the surface, and age of the solution; which all change the deposited layer thickness. Under these conditions different factors play a role in this process such as surface cleaning, deposition conditions such as temperature and humidity, and time between depositing the material on GaAs and annealing. To eliminate the effect of these parameters on the process, the deposition process was done inside class 100 clean room, consistent cleaning procedure and fixing the time between depositions and annealing. After the optimization process the conditions

that produced the best transmission spectra were fixed and applied on real devises. As a comparison the transmission spectra of SiO_2, ZnS, ZnO and MgF_2 were plotted together and shown in Figure 6.2 (d). It has been noticed that the transmission spectra for the samples coated are better than the pristine GaAs transmission. The enhancement for the different materials is on the order of 35 %. The increase in the transmission is direct evidence of the increasing number of photons passing through the GaAs. In other words the GaAs surface reflection reduced by about 35 % than the original case without coating.

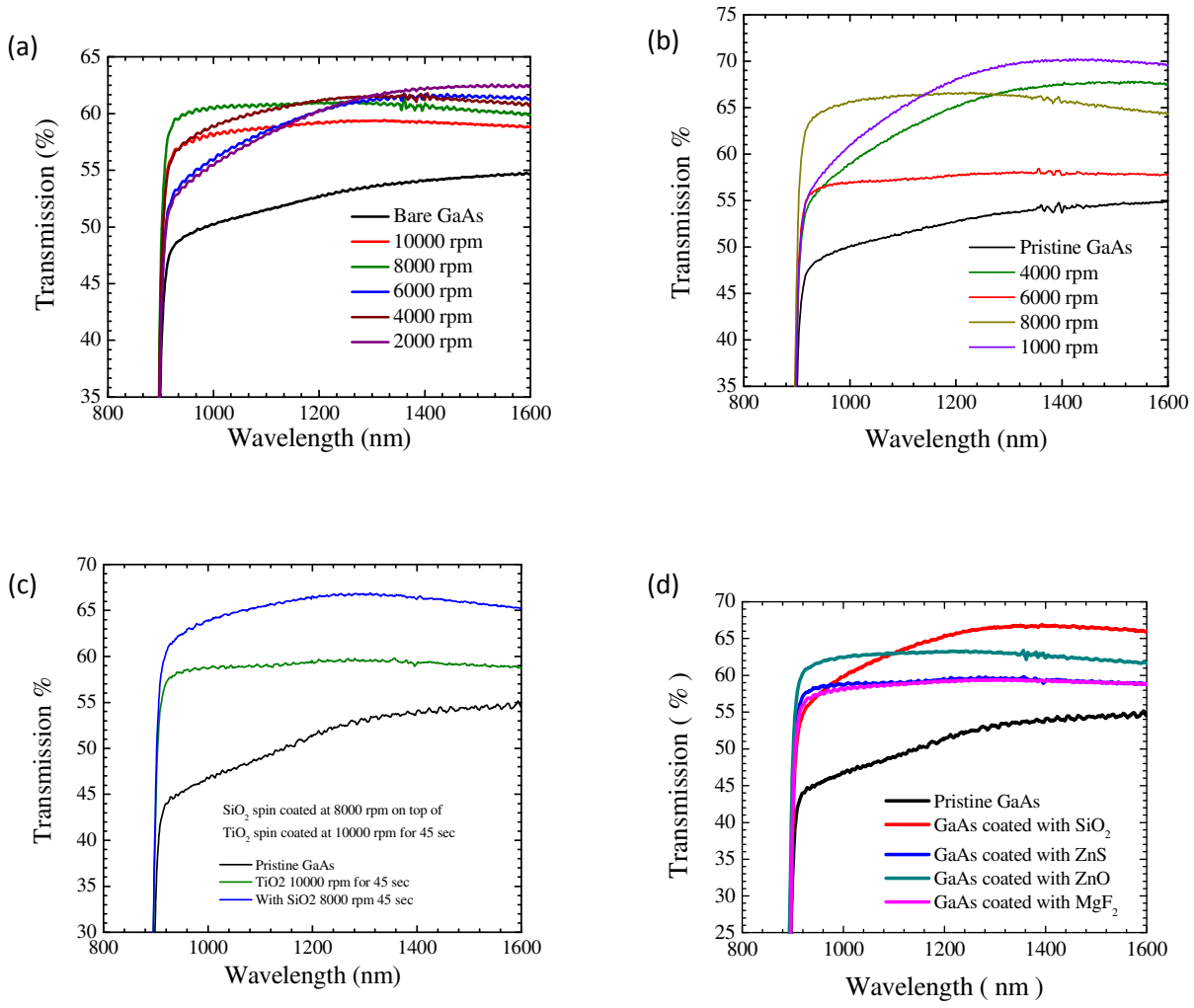

Figure 6.2. Transmission spectra of semi-insulating GaAs after coating with (a) Zinc oxides at different speeds, (b) ZnS at different speeds, (c) TiO_2 and SiO_2 bilayer, (d) Transmission of GaAs coated with different materials comparison.

Raman and X-ray Diffraction Measurements

Both Raman and X-ray diffraction were performed to confirm the formation of the grown compounds. Since each material has different Raman and XRD spectra each grown material can be measured using these two methods. Then the spectra obtained from each test can be compared to published results. It is important to mention here that at low annealing temperatures the crystallinity of the materials is not high; hence it is not an easy task to perform these measurements. Both measurements were performed after coating and annealing the samples. The Raman results were obtained by using a blue laser with 472 nm wavelength for all the materials. Both Raman and XRD spectra obtained for ZnO are shown in figure 6.3 [29].

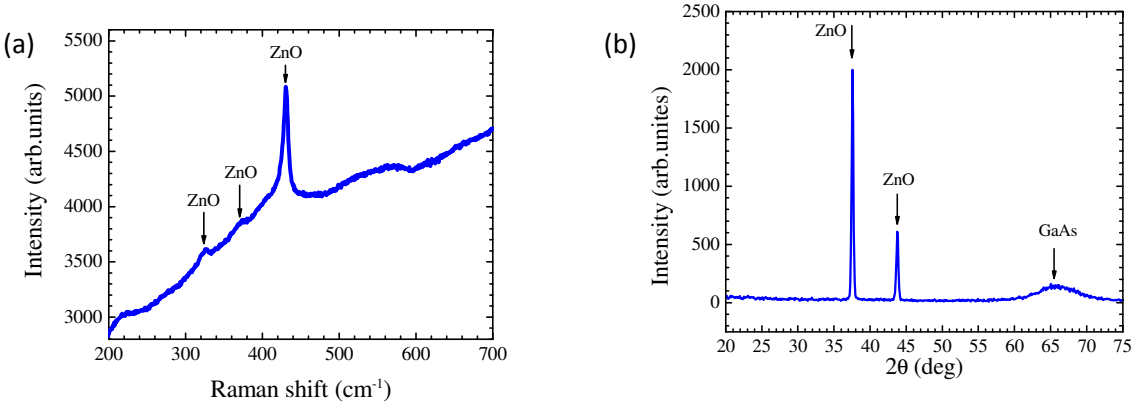

Figure 6.3. (a) Raman spectra of ZnO coated on GaAs, (b) X-ray diffraction of ZnO coated on GaAs. Reprinted with permission from Makableh *et al*

Three main peaks were observed for ZnO from the Raman data, these peaks are at 324, 376 and 430 cm^{-1}. From the XRD spectrum it noticed two peaks at 37.4° and 43.7° which both are ZnO peaks according to XRD materials library. Both spectra show peaks that are consistent with published reports [94], [95]. To further investigate the other low refractive index materials; Raman spectra were obtained for SiO_2, and MgF_2. The Raman spectra for these materials are

shown in figure 6.4 (a, b). Some of the other undefined peaks in both spectra might be due to impurities in the deposited materials.

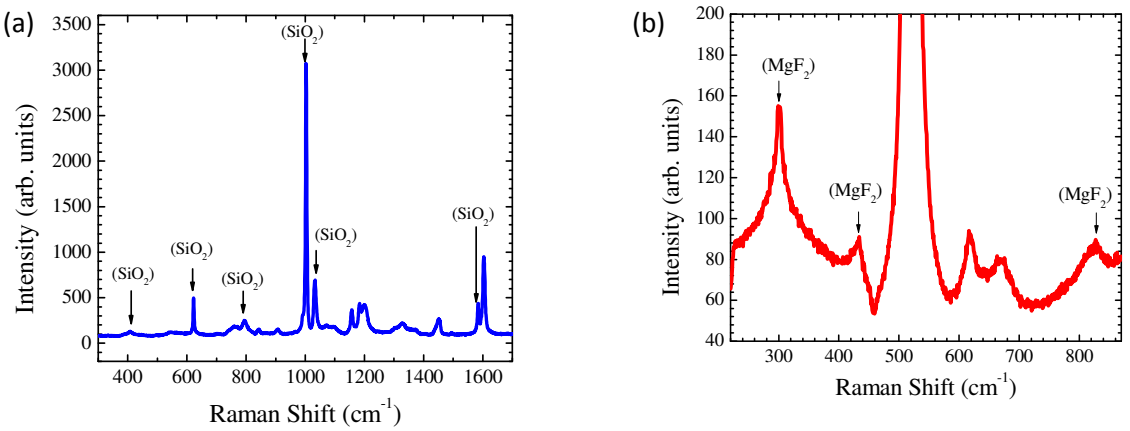

Figure 6.4 Raman spectra of (a) Silicon dioxide sol-gel coated on GaAs, (b) Magnesium Fluoride e-beam deposited on GaAs.

Reflection Measurements

Reflection measurements were performed for ZnO to obtain the reflection of the coated samples with ZnO compared to pristine GaAs. Also from this test, the refractive index was obtained in the spectra range of interest for GaAs. Both surface reflectance before and after coating GaAs with ZnO and the refractive index of ZnO on top of GaAs are shown in figure 6.5. It is also mentioned that the reflection reduced by 35 % which is consistent with the transmission results as discussed before. The calculated refractive index of ZnO is around 1.65, which is closed from published results of 1.9 – 2. The difference in the refractive index of the ZnO layers used in this project and other reposted results is due to the low annealing temperature used for these samples. The annealing of these samples was fixed at 150 ^{o}C. This temperature does not completely transfer the ZnO to crystalline structure, but it was enough to have good quality for ZnO according to the materials characterization performed on ZnO.

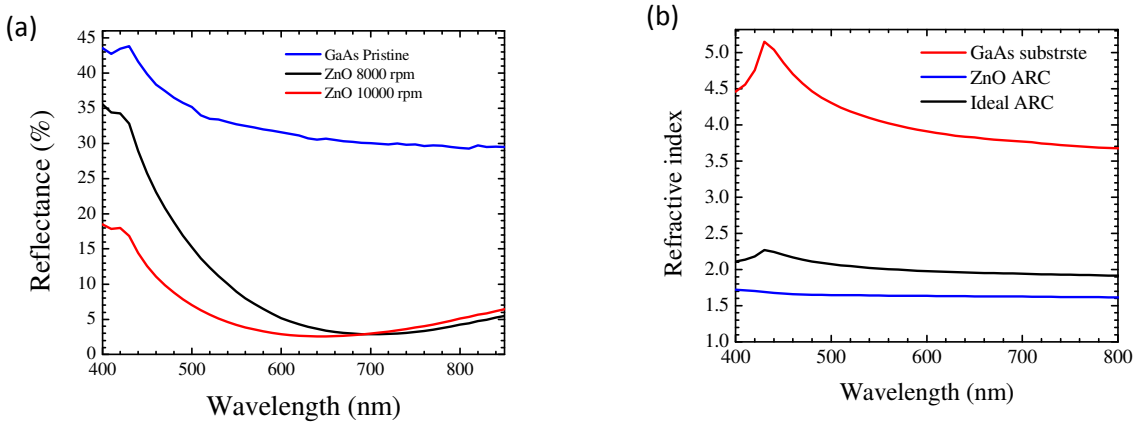

Figure 6.5. (a) Reflectance of GaAs before and after coating with ZnO at 8000 rpm. (b) Refractive index of ZnO coated on GaAs, compared with ideal refractive index for GaAs anti-reflection coating [29]. Reprinted with permission from Makableh *et al*

C. Device Enhancement due to Anti-Reflection Coating Effect

After the materials characterization was completed, several devices were used to investigate the ARC on them. First the devices were characterized using IV, EQE and spectral response measurements before coating. Then the devices were characterized using the same three methods after coating. As a result, the enhancement due to the ARC can be studied. The conditions to coat the devices with the ARC materials were selected from the previous measurements. The selection criteria were according to the following:

1. Spin coating speed that gives best transmission and less reflection on semi insulating GaAs. In general speeds (~ 8000 rpm) were giving the best results according to this criteria.
2. Annealing temperature. The best annealing temperature found to be 150 ^{o}C from the experimental results. This temperature was chosen since it does not affect the solar cell

junction, enough to evaporate the organic compounds from the coated materials and to give high quality coated layers.

3. Surface morphology. It is very important to have full surface coverage, and to be contamination free. This was guaranteed by using the synthesis materials within their expected life time and to use clean room for the deposition process.

Current-Voltage Characteristics

After the best coating conditions by investigating the effect of ARC on both absorption and reflection on semi insulating GaAs, different solar cells were coated with the ARC materials. The solar cells were characterized before and after coating with ARC. This type of characterization can give the enhancement in the power conversion efficiency due to using anti-reflection coatings on them. The measurements carried out at room temperature. Since the effective area for each solar cell is known, both power density and current density were used in the calculation. In the following discussion, the results obtained for solar cells coated with ZnO, TiO_2, ZnS, MgF_2 and SiO_2 are presented.

Zinc Oxide was used to coat two different solar cells. The first cell was a pm junction GaAs reference cell, and the second cell was quantum dots solar cells with 15 % In mole fraction structure. In order to verify the optimization process that's was done on semi insulating GaAs is valid for the solar cells only, different pn junction solar cells were coated with ZnO at different speeds while maintain annealing temperature at 150 ^{o}C. The IV characteristics obtained for the optimization process on solar cells are shown in figure 6.6 (a) [29], and in figure 6.6 (b) the solar cell surface color change after coating it with ZnO compared to pristine cell.

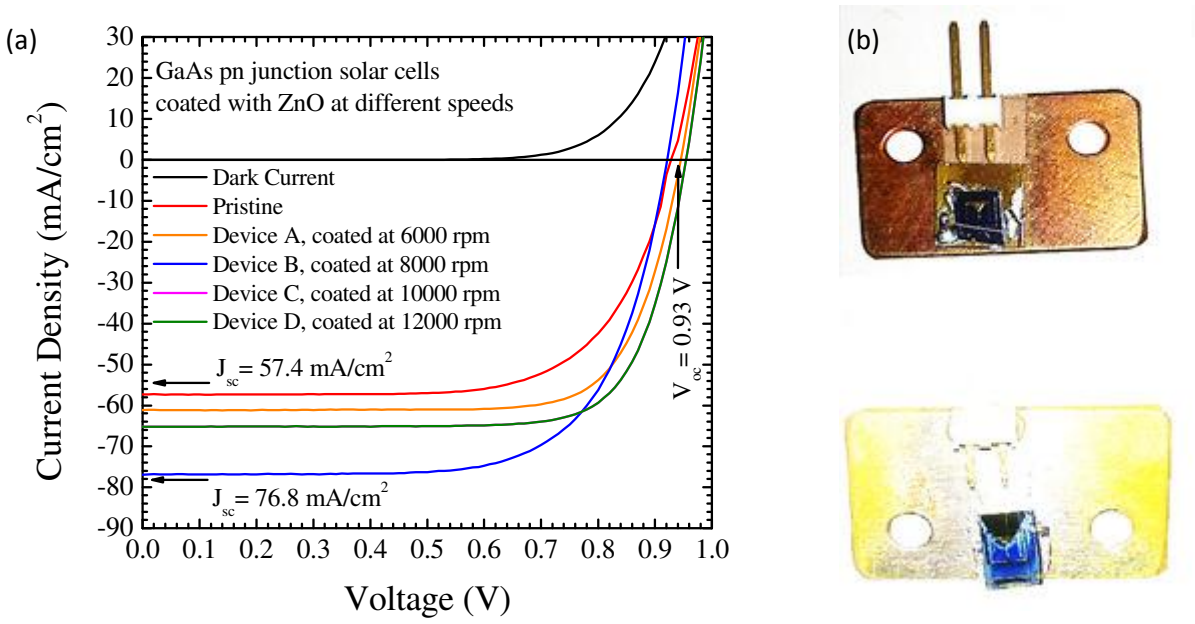

Figure 6.6. (a) The IV characteristics of different solar cells coated with ZnO at different speeds [29]. (b) Solar cell surface color change before coating top picture, and after coating with ZnO lower image "Photo by Yahia Makableh". Reprinted with permission from Makableh *et al*

From the optimization process, it is apparent how the spin coating speed plays a major role in changing the solar cell characteristics. This is due to coating layer thickness on top of the solar cell, which is in direct relationship to the spin coating speed. It is also mentioned the major enhancement in the photocurrent generation after coating the solar cells with ZnO. As shown in the figure the best enhancement is obtained from the device coated with ZnO at 8000 rpm. In this case the short current density J_{sc} changed from 57.4 mA/cm^2 before coating to 76.8 mA/cm^2 after coating. For the power conversion efficiency η changed from 9.2 % before coating to 12.25 % after coating. Both the short circuit current density and power conversion efficiency faced enhancement of 34 % and 35 %, respectively. This enhancement is in the same order found for both reflection reduction, and GaAs transmission enhancement. Also from the IV characteristics, there is no significant change in the open circuit voltage (~0.93 V), thus the

enhancement in the power conversion efficiency is due to more carrier generation after enhancing the solar cell absorption.

After the optimization process, the ZnO coating was applied on InAs/$In_{0.15}Ga_{0.85}As$/GaAs quantum dots solar cell. Both IV characteristics for the GaAs reference cell coated with ZnO at 8000 and for the quantum dots solar cell coated at 8000 rpm are shown in figure 5.6

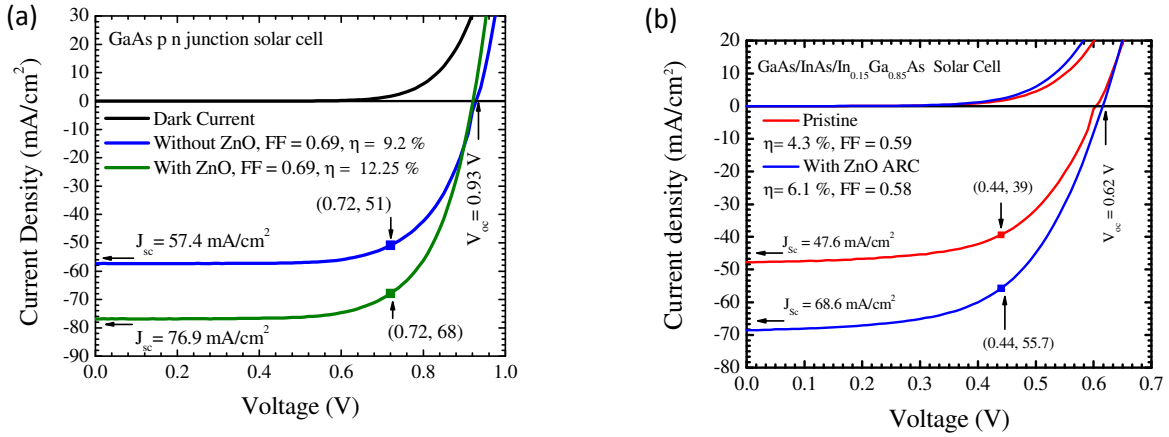

Figure 6.7. Current-Voltage characteristics of ZnO coated on top of (a) Reference GaAs pn junction solar cell, and (b) InAs quantum dots solar cells [28] [29]. Reprinted with permission from Makableh *et al*

In comparison to the reference solar cell which enhanced about 35 % after coating with ZnO, the quantum dots solar cell enhanced by 41 %. The better enhancement in the quantum dots solar cells is due to the enhanced response of the quantum dots in the near infra-red region. The quantum dots enhanced response will be discussed later in sections. The filling factor and the open circuit voltage did not change in both solar cells, which validate the ability of the ARC to enhance the photocurrent generation, hence enhancing the power conversion efficiency.

To further investigate the effect of other ARC with high refractive index materials on GaAs solar cells, TiO_2, ZnS were also used. The IV characteristics obtained by coating pn

junction solar cells with TiO_2 and ZnS are shown in figure 6.8. Both cells show significant enhancement after applying the ARC to them. The enhancement in the power conversion efficiency due to using TiO_2 ARC is on the order of 49 %, and in ZnS is on the order of 29 %. The higher enhancement seen in TiO_2 compared to ZnS is due to the formation of the coated layer on top of the solar cell. Also, the ZnS has lower refractive index compared to that of TiO_2, which also plays a major rule in the lower enhancement from using ZnS compared to TiO_2. The thicknesses of these materials found to be around 80 nm thick by using Ellipsometry characterization.

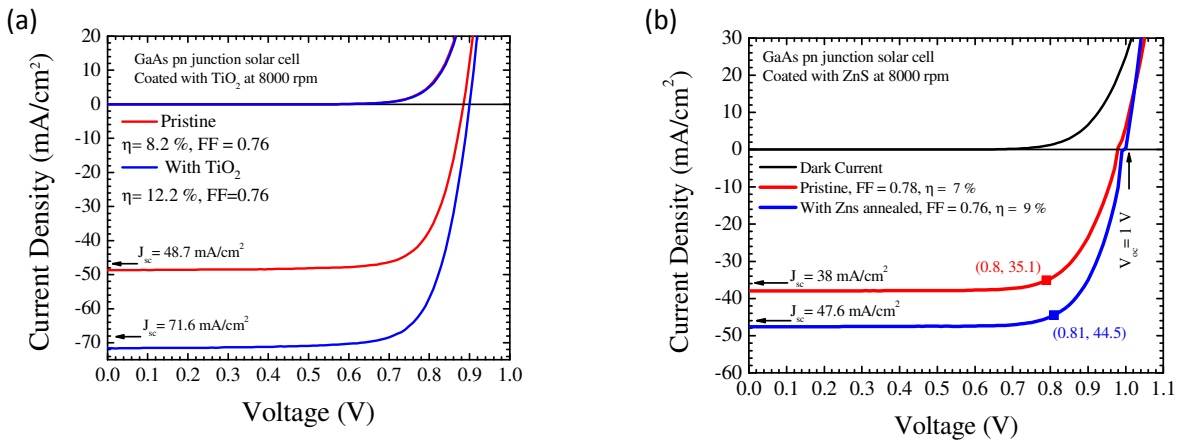

Figure 6.8. Current-Voltage characteristics of (a) GaAs reference cell coated with TiO_2, and (b) GaAs reference cell coated with ZnS.

After the application of the higher refractive index ARC materials on different solar cells, lower refractive index materials were used. These two materials are SiO_2 and MgF_2 with refractive index for each around 1.4. Due to lower refractive index both materials supplied enhancement to the solar cells power conversion efficiency on the order of 22 - 25 %. This is due to the fact that their refractive index falls below the best ARC refractive index value of 1.92 for GaAs. Therefore, these two materials are better used as a second layer in designing multi-

layer anti-reflection coatings for these solar cells. The IV characteristics for solar cells before and after coating them with SiO_2 and MgF_2 are shown in figure 6.9. For these lower refractive index materials the deposited layer has to have higher thickness than higher refractive index materials. From the optimization process SiO_2 best speed was found to be 7000 rpm, which gave a thickness of around 120 nm by using Ellipsometry measurements. The same thickness was used for MgF_2. The MgF_2 was deposited by using electron bean evaporation of MgF_2 pellets; due to the difficulty of synthesize MgF_2 without using highly toxic gases.

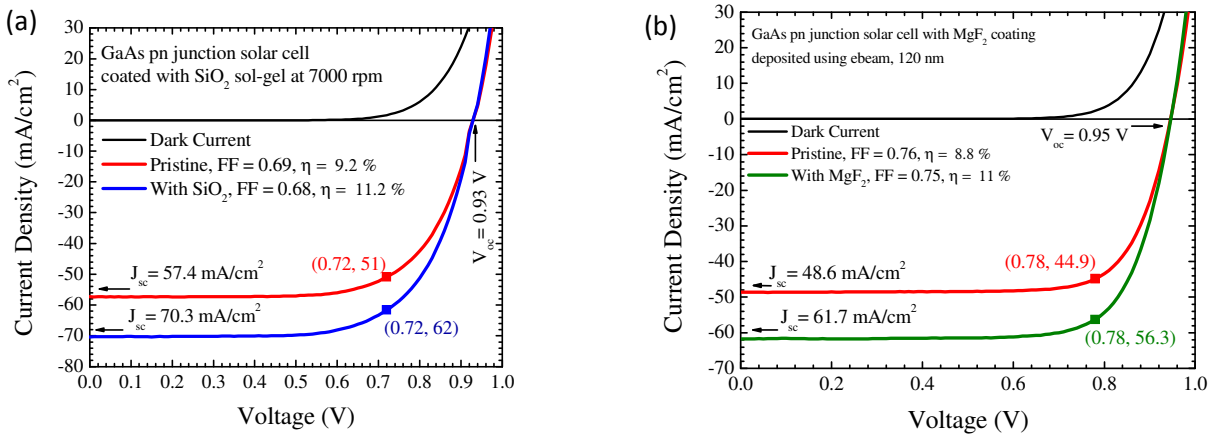

Figure 6.9. Current-Voltage characteristics of (a) GaAs reference cell coated with SiO_2, and (b) GaAs reference cell coated with MgF_2.

External Quantum Efficiency Characterization

External quantum efficiency measurements were performed for all the solar cells before and after coating them with ARC layers. The measurements were done at room temperature, and in the spectral region between 400 – 1200 nm. The tests were done at 5 nm resolution, which is the highest resolution the Oriel IQE200 system can reach. Since the EQE test has direct relationship with the number of absorbed photons and their ability to generate electrons, then any increase in the number of absorbed photons supposed to increase the generated electrons, leading

to enhanced EQE spectra. The spectra of the different cells were significantly enhanced after using the ARC, so the experimental results in agreement with the expected output. The EQE spectra acquired from the pn junction solar cell and the quantum dots solar cell coated with ZnO are shown in figure 6.10. Around 50 % improvement in the EQE spectra was noticed in the solar cells. On the other hand, the quantum dots response has shown increase as well after coating the quantum dots solar cell with ZnO. The increased response is a direct measure of the ability of this ARC to better the performance of the solar cell device.

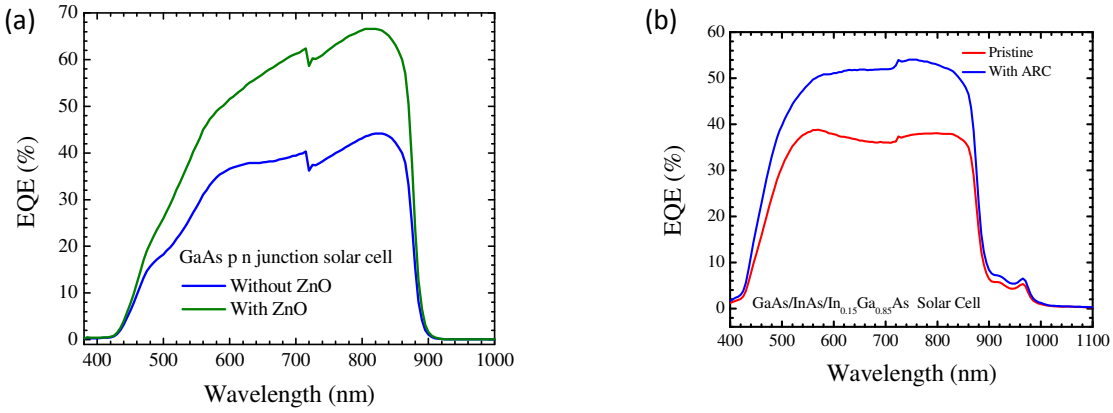

Figure 6.10. External Quantum Efficiency spectra of (a) GaAs reference cell coated with ZnO, and (b) InAs quantum dots solar cell coated with ZnO [28] [29]. Reprinted with permission from Makableh *et al*

Similarly, the EQE spectra of pn junction GaAs solar cells coated with TiO_2, ZnS, SiO_2 and MgF_2 are shown in figure 6.11. All solar cells coated with ARC have improved in similar fashion seen in the IV characteristics.

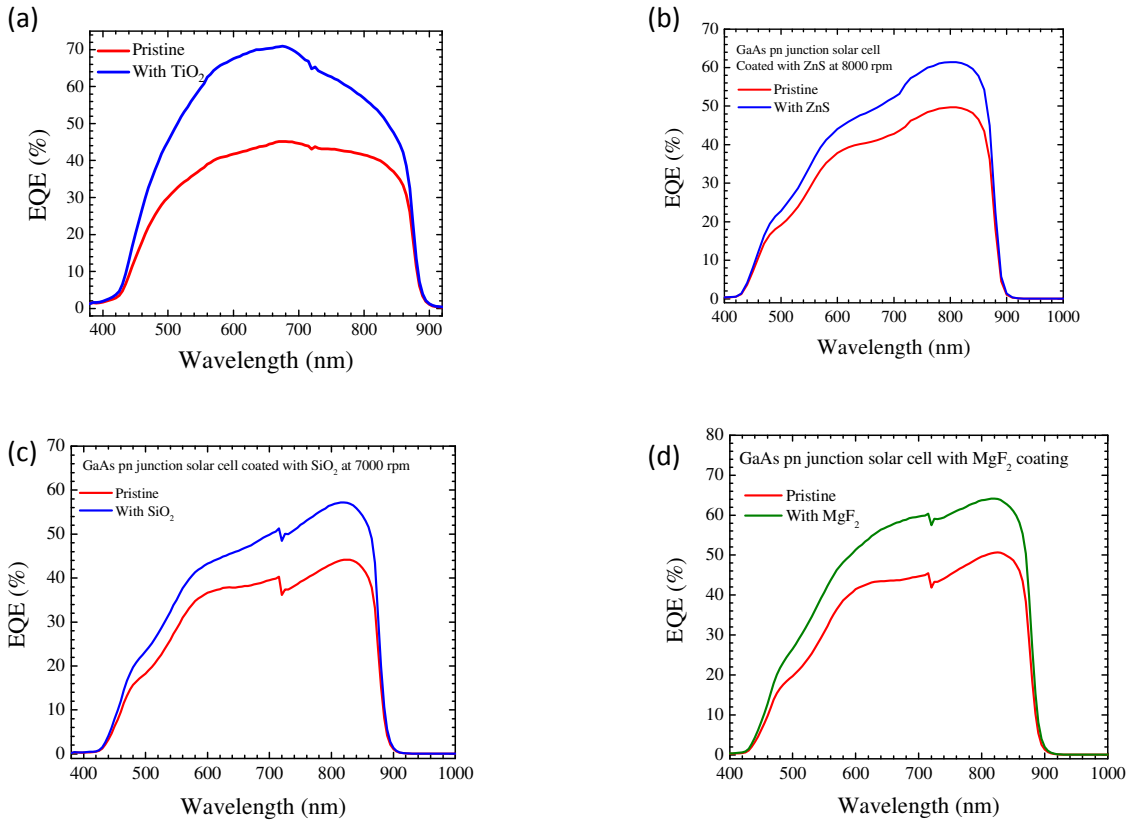

Figure 6.11. External Quantum Efficiency spectra of GaAs pn junction reference cells coated with (a) TiO_2, (b) ZnS, (c) SiO_2, and (d) MgF_2

Spectral Response Measurements

The third important type of characterization done to the solar cells is Spectral Response measurements. The spectral response of all solar cells was obtained before and after coating the solar cell between the range 400 nm – 1200 nm. The spectra response of both the reference pn junction cell and the quantum dots cell are shown in figure 6.12. It is noted the significant enhancement seen in the spectral response spectra after coating the samples with ZnO. In comparison between both spectra, the largest enhancement seen at 865 nm in both cells that is on the order of 35 % for the reference cell and 40 % for the quantum dots cell.

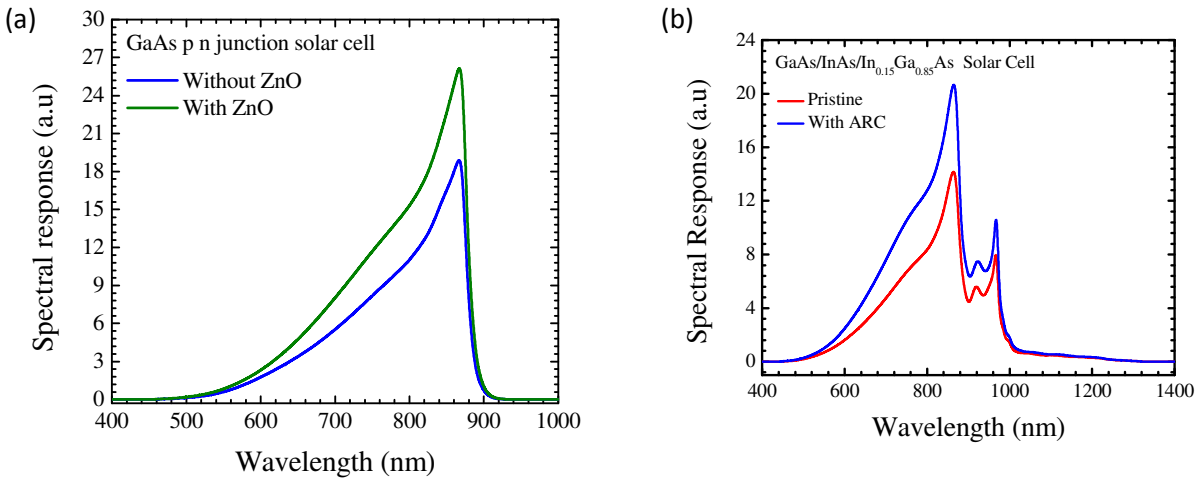

Figure 6.12. Spectra Response spectra of (a) GaAs reference cell coated with ZnO, and (b) InAs quantum dots solar cell coated with ZnO [28] [29]. Reprinted with permission from Makableh *et al*

From all the measurements have been performed for the solar cells before and after coatings, the device performance has improved in all the solar cells. The IV characteristics the better response is related to the increased photocurrent generation, while the open circuit voltage is fixed in all solar cells. Additionally, both the EQE and spectral response have direct relationship with the photocurrent generated, therefore all the improvement in these solar cells is only related to the increased photocurrent generated after using the ARC. The increase in the solar cell performance is then related to the decreased transmission from the solar cell surfaces.

VII. Hydrophobic Treatment Using Surface Nanotexturing

A. Introduction

Surfaces with self-cleaning properties are very important in several applications such as coating glass in high buildings to reduce the need of cleaning the glass panels, also in solar cells where these cells can be placed in remote places. Beside this the large number of applications that have been found after discovering this feature. Adding this feature through nanotexturing to solar cells is very interesting especially when this modified surface can act as an anti-reflection coating. In this project anti-reflection coating/superhydrophobic surface has been the core of the research. This has been obtained first by growing ZnO nanoneedles on top of the solar cells using hydrothermal growth, then by treating the nanoneedles with fatty acids. The fatty acid is capable of reducing the surface tension from high surface tension to low surface tension. The transfer is done by assembling several layers of carbon chains on the surface. Each layer can be considered as a monolayer. The carbon monolayers can act as a waxy surface, which is water repellent surface.

The treatment of ZnO for hydrophobicity is done through using stearic acid. This acid is the most saturated acid can be found in nature; by containing 18 carbon molecules in its carbon chain. Stearic acid is nontoxic, cheap and easy to used compared with other methods of obtaining hydrophobic surfaces. The toxicity of this acid is very low or can be considered nontoxic as it is obtained from animal's fat. So this way of surface modification can be considered environmental friendly, beside its cheap cost that may allow mass production in the future. In the following discussion both growth of ZnO nanoneedles and treating the nanoneedles for hydrophobicity will be discussed in details.

B. Growth of Zinc Oxide Nanoneedles

The growth of the ZnO nanoneedles is done through hydrothermal growth method. First the solar cell is coated with ZnO seed layer. The seed layer is prepared in the same way as the ZnO sol-gel solution for ARC. The only difference between the sol-gel for ARC and for seed layer is that the ones used for seed layer has lower molarity (~0.25 M). This molarity can give much less thicknesses than the one used for anti-reflection coating. Generally, the thickness of the seed layer is between 5 nm – 20 nm thick layer, compared to 80 nm – 100 nm thick layer for ARC. The lower thickness is needed in order to minimize surface roughness, and to grow nanoneedles with diameters around 50 nm. Higher molarity seed layers or higher seed layer thicknesses can change the alignment of the nanoneedles and their diameter size. The seed layer is spin coated on top of the solar cell at 4000 rpm. After the cell coated with seed layer, it is annealed in open air at 175 ^{o}C for 30 minutes. Following annealing no further process to the cell itself is done tell it is immersed in the growth solution at 92 ^{o}C for three hours.

The ZnO nanoneedles growth solution is prepared by mixing a 1:1 molar solution of Zinc Nitrate and hexamethylenetetramine (HMTA). The Molarity chosen here is 0.025 Molar for both solutions. This is achieved by dissolving 0.148745 gm of Zinc Nitrate Hexahydrate in 10 mL DI water and 0.070093 gm in 10 mL DI water. Both solutions were pre stirred at 400 rpm for 90 minutes. After pre mixing, the HMTA solution was added slowly to the Zinc Nitrate solution, then the total mixture is stirred at 400 rpm for 60 minutes. While stirring Ammonium Hydroxide was added to the mixture to raise the pH to 10. High pH value is needed to etch the tip of ZnO nanorods to obtain nanoneedles. When the stirring process is finished the mixture

was filtered by using 0.2 μm filters to remove any particles that were generated during the stirring process. The growth process was completed by immersing the solar cell inside the solution in a tilted position 32^{o} facing down. After three hours of growth time, the growth solution is then set to cool down naturally to room temperature. Sample cleaning is followed by immersing and shacking the cells in fresh DI water between 6-10 times to remove any growth solution residuals. Post annealing at 175 ^{o}C for 60 minutes in open air is the final step.

After growing the ZnO nanoneedles on the solar cells, both Raman spectra and surface morphology using SEM were obtained. The Raman spectra give information about the ZnO nanoneedles quality. The spectra were obtained by using blue laser in the range between 330 cm^{-1} and 500 cm^{-1}. This range was selected to eliminate the Raman response from GaAs, which is much stronger than the ZnO response bellow 330 cm^{-1}, that if presents makes the ZnO peaks to be very small. The upper limit was set to eliminate the peaks that could present from oxygen in oxide structures in general. The Raman spectra obtained from grown ZnO nanoneedles on GaAs is shown in figure 7.1. In comparison with the Raman spectra of ZnO ARC obtained before, the Raman for the nanoneedles have excellent match.

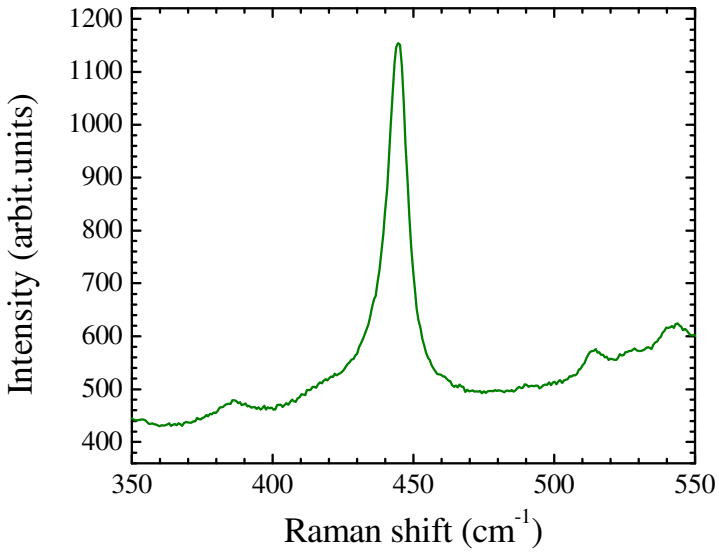

Figure 7.1. Raman spectra of ZnO nanoneedles grown on top of GaAs

After obtaining the Raman spectra for grown nanoneedles and nanorods surface morphology was obtained for different samples by using scanning electron microscopy. From the SEM images different information can be gathered about the nanoneedles such as surface coverage, length and diameter of the nanoneedles. Scanning electron microscopy images were taken for different samples are shown in figure 7.2. The SEM images show excellent surface coverage, and highly aligned structures. This can be related to the well-controlled seed layer deposition, and to the controllability of the growth process. The average length from the nanoneedles was found to be 1 μm, and the average diameter is around 100 nm.

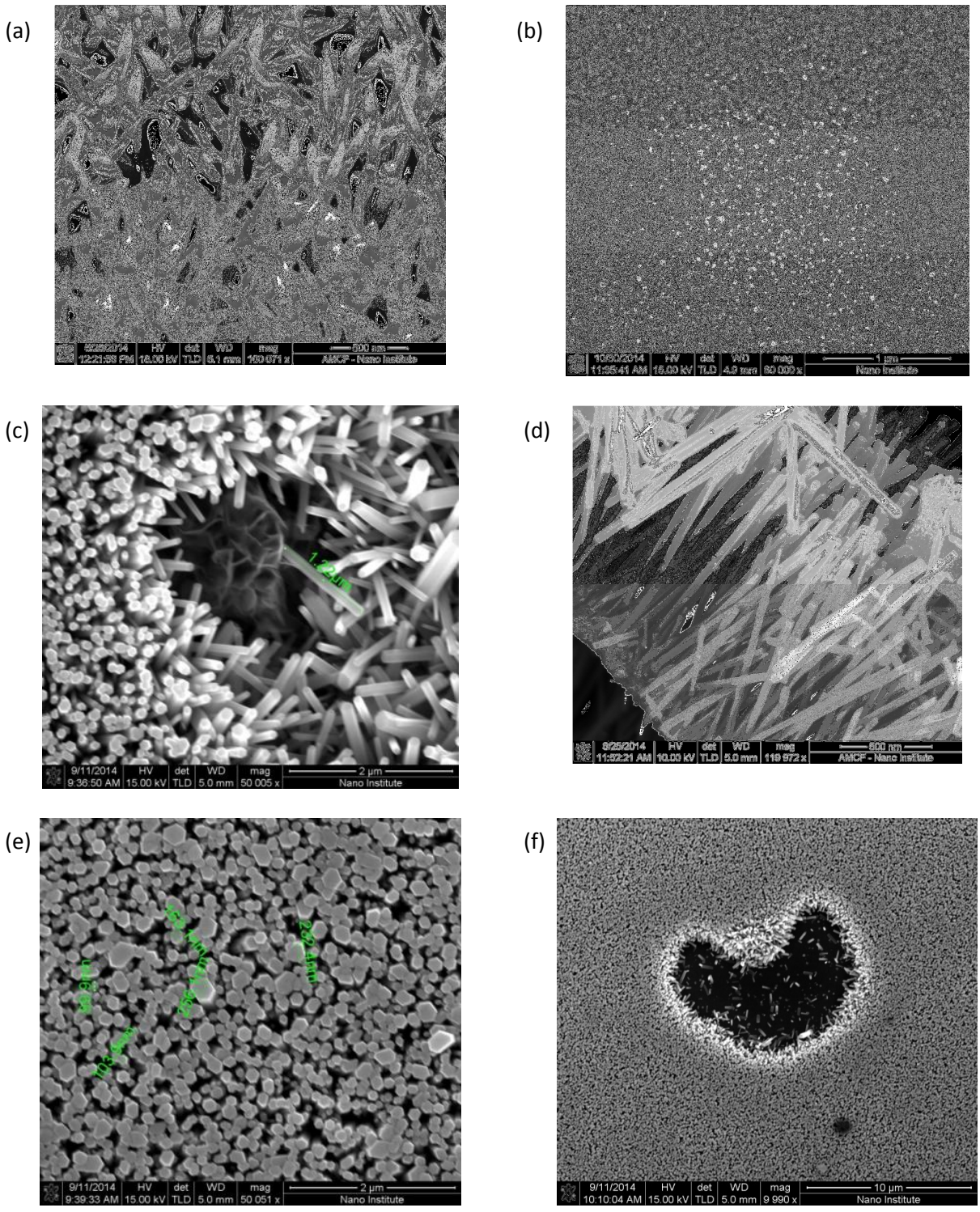

Figure 7.2. Scanning electron microscope of ZnO nanostructures grown on GaAs.

C. Surface Treatment for Hydrophobicity Properties

The treatment of the ZnO nanostructures for hydrophobic properties takes place after the growth is completed and the nanostructures are characterized. This process is done by preparing 20 mL of 10 mM Stearic Acid ethanolic solution by dissolving 0.014224 gm of Stearic Acid to 20 mL of Ethanol. To enhance the solubility of the Stearic Acid in Ethanol, the solution is set in sonication bath at 45 ^{o}C for 30 minutes. Then the solution is cooled down to room temperature. The solar cells with nanoneedles on top of them are then immersed in the solution for 24 hours. After 24 hours, the solar cells were then immersed in Ethanol to remove and residuals from the surface and annealed in furnace at 100 ^{o}C for 2.5 hours. The cells were then set in a clean environment in open air for 12 hours before testing.

Contact angle measurements were taken for the solar cells after the hydrophobic treatment. It was found that the contact angle of a 10 µL water droplet is around 156^{o}, which is superhydrophobic [72], [77]. The image showing the contact angle measurements is shown in figure 7.3. The test was performed in dynamic mode by using 10 µL water droplet. Dynamic test was used as the surface was showing superhydrophobicity and did not allow smaller water droplets to be used in static mode.

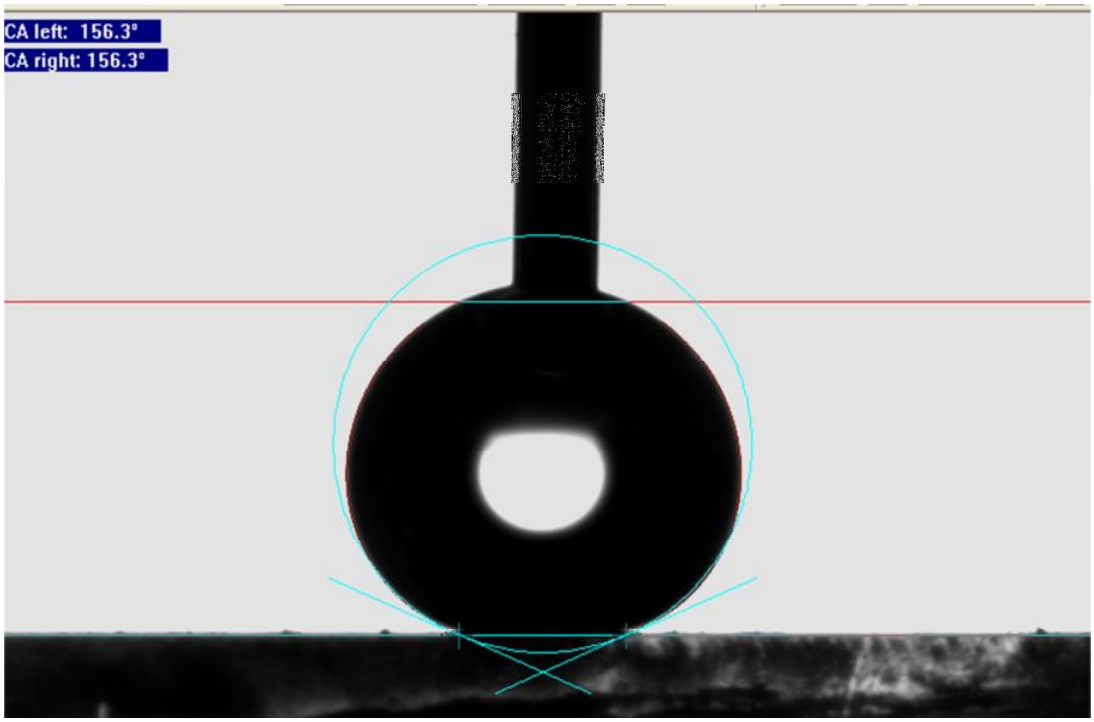

Figure 7.3. Contact angle measurement of ZnO nanoneedles treated sample with Steric Acid.

D. Solar Cells Anti-Reflection/Superhydrophobicity Surface

Solar cell surface modification was performed to give it ARC and hydrophobic properties at the same time. For this purpose ZnO nanoneedles were first grown on an InAs quantum dots solar cell. The grown nanoneedles were then treated for hydrophobicity by using the same method discussed in before. All device characterizations were performed before and after the surface modification. The IV of the treated solar cell is shown in figure 7.4. The red curve shows the photocurrent of the pristine cell before any treatment. Both the blue and the green curves show the photocurrents after ZnO nanowires growth and hydrophobicity treatment, respectively. A significant enhancement in the power conversion efficiency was observed after modifying the cell surface with nanowires. The enhancement is on the order of 48 %. This increased performance is related to the increased photocurrent generation due to the anti-

reflection coating effect. There is no significant increase in the efficiency after hydrophobicity treatment. Also, the cell performance was not decreased after hydrophobicity treatment, hence this surface modification show dual functional surface that is serving as an anti-reflection and self-cleaning surface at the same time. A slight increase in the open circuit voltage (~ 20 mV) was noticed, this increase could be related to enhanced surface collection and metal contact quality during the different processes. The filling factor of the cell did not change and the open circuit voltage was almost the same after the modifications (~ 0.6 V), therefore, the increase in the power conversion efficiency is due to the increased photocurrent generation.

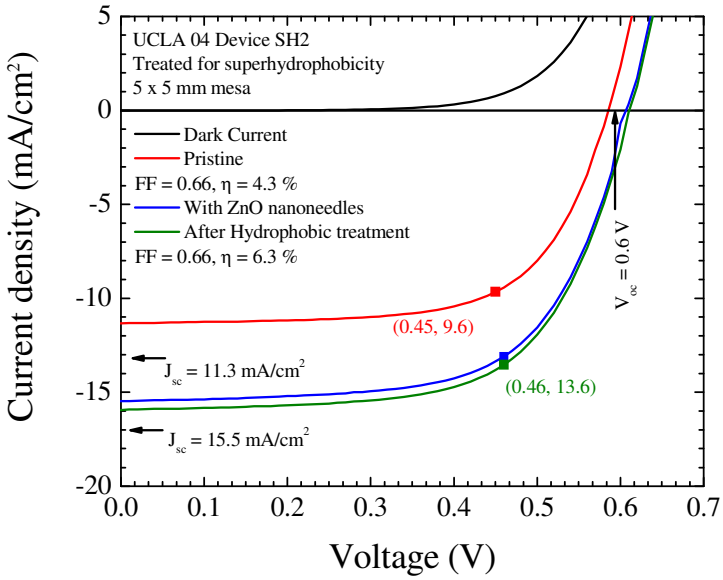

Figure 7.4. Current-Voltage characteristics of InAs quantum dots solar cell after surface modification for anti-reflection coating/hydrophobic surfaces.

The external quantum efficiency spectra were acquired for the cell before and after surface modification. The EQE spectra are shown in figure 7.5. The EQE spectra were increased after the surface modification. The highest increase in the spectra was seen at 810 nm and is on the order of 43 %. The response from the quantum dots can be also be noted at 925

nm. The quantum dots response also increased after the surface modification. In general the EQE spectra was improved over the entire GaAs and InAs response.

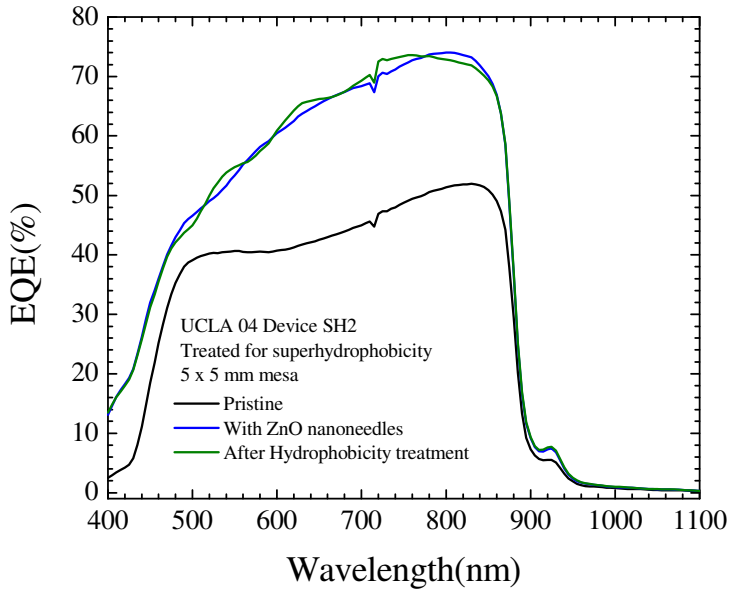

Figure 7.5. External quantum efficiency spectra of the InAs solar cell after surface modification.

To have a complete picture about the cell performance spectral response measurement was also performed. The spectra response spectra before and after solar cell surface modification are shown in figure 7.6. The spectra were also improved over the entire cell response. The response from the GaAs was increased on the order of 41 %. On the other side, the InAs quantum dots response was improved significantly on the order of 34 %. The spectral response results are in good match with the IV and EQE results. Also the InAs response is in good match with the EQE results.

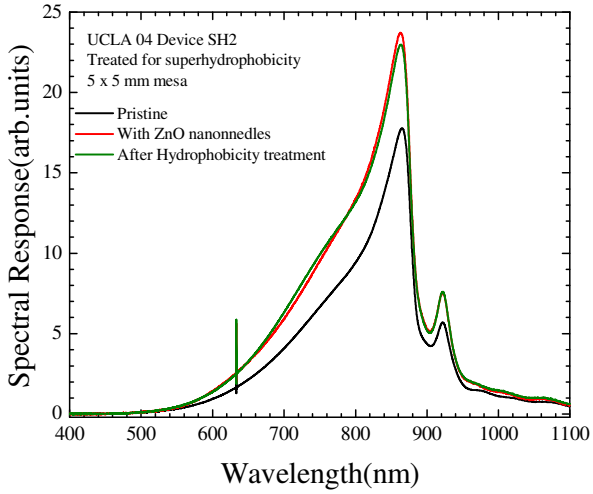

Figure 7.6. Spectral response spectra enhancement after the solar cell surface modification.

The contact angle measurement for the hydrophobic surface was measured and found to be ~ 153^{o}. Since the contact angle is higher than 150^{o} the surface is considered a superhydrophobic surface [72], [77]. The image showing the water droplet during the contact angle measurements is shown in figure 7.7. From all the device characterization, it is noted how the solar cell device performance increased remarkably after the surface modification. Moreover, the hydrophobicity treatment did not affect the anti-reflection coating effect. Henceforth, a dual function surface is achieved in this process. The enhanced performance is due the ARC affect that led to increased light absorption in the solar cell junction.

(a)

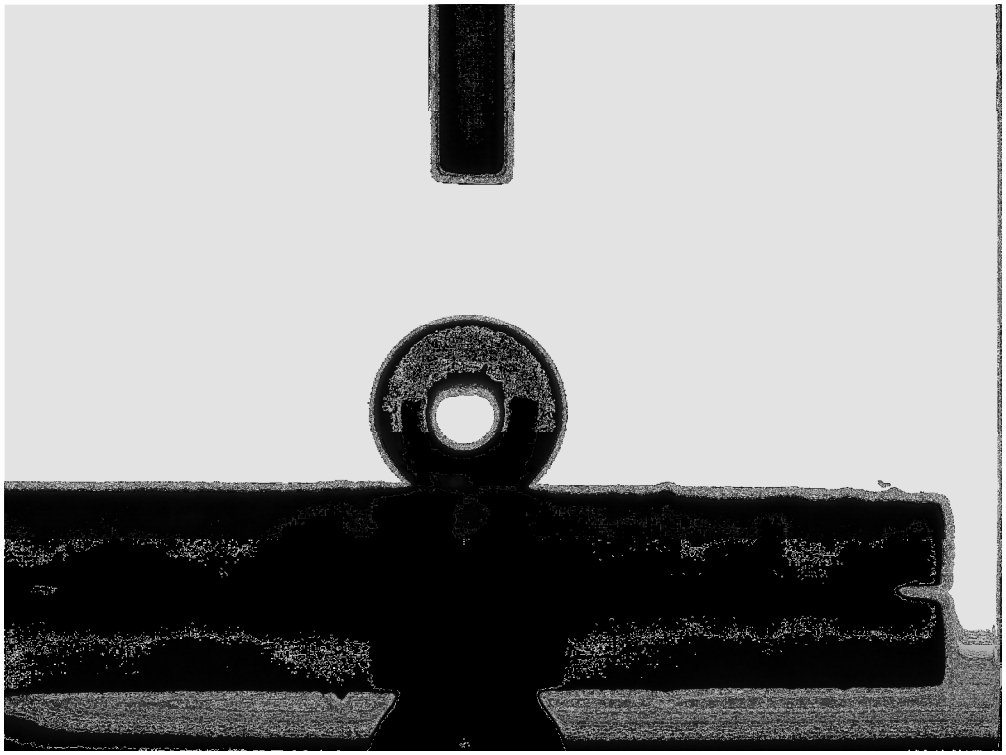

(b)

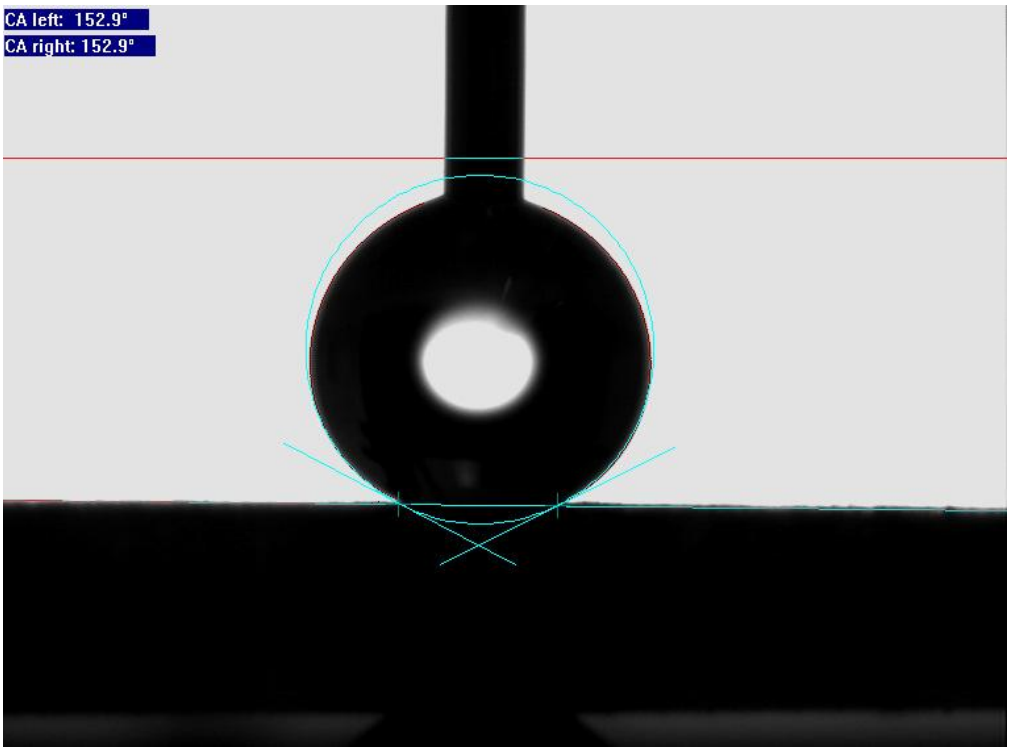

Figure 7.8. Contact angle measurements for a 10 μL water droplet on the solar cell treated surface.

VIII. Conclusion and Future Research

A. Conclusion

In conclusion, performance enhancement of GaAs based photovoltaic devices has been investigated. Three approaches were followed, the first one was to change the design of the GaAs pn junction by adding InAs/$In_xGa_{1-x}As$ quantum structures and changing the Indium mole fraction x. The second approach was done coupling Plasmonic nanoparticles to the solar cells. The third approach was achieved by anti-reflection coating/hydrophobic dual function surface modification. The performance of the devices was assessed by using Current-Voltage, External Quantum Efficiency and Spectral Response measurements. The device structure modification shows extended device response beyond the GaAs bandgap. The extended response is related to the InAs quantum dots used in the device structure. It was observed that the short circuit current increased in the quantum dots devices compared with the pn junction reference cell. Despite the increased short circuit current, the device power conversion efficiency dropped due to reduced open circuit voltage. This reduction is related to both the reduced bandgap of the cell after using the InAs structures, and due to the lattice mismatch between the InAs and GaAs.

The evolution of the Plasmonic nanoparticles effect on the solar cells revealed enhanced response on the order of 15 %, as seen in the cells characteristics. The higher device performance was seen with the colloidal grown nanoparticles. Also, e-beam deposited nanoparticles were used to study their effect on the cells. This method did not affect the device performance as mentioned in the Current-Voltage characteristics.

On the other hand, significant device performance enactment was mentioned after using anti-reflection coatings. The enhancement is on the order of 40 – 50 % compared with untreated devices. The anti-reflection materials were synthesized using sol-gel method, and/or deposited

with e-beam deposition. The anti-reflection coating materials and their effect on GaAs were characterized using Transmission, absorption, reflection, Raman and XRD microscopy. Furthermore, superhydrophobicity was achieved though surface treatment with Stearic Acid. The surface treatment was performed on ZnO nanostructures grown on the devices. The treated surfaces were characterized using Scanning Electron Microscopy and contact angle measurements. A contact angle of 153^{o} was achieved on the treated devices. Additionally, an increased response was observed in the InAs quantum dots after using the anti-reflection coating surface modification.

B. Future Work

The extended response of the InAs quantum dots beyond the bandgap of GaAs is promising to achieve higher efficiencies. In order to eliminate the reduced open circuit voltage other strain compensation layers can be used between the InAs and the GaAs. This can be done through changing the growth method from MBE to MOCVD. Additionally, other Indium concentration and quantum dots designs can be used to extend the response more towards the near infra-red region. In addition to the device structure changes, the surface modifications can be optimized and further processed to investigate the use of bilayers of two different types of nanostructures. This can be accomplished by coupling SiO_2 nanoparticles to ZnO nanorods and investigate their effect on the device performance. Other surface modification techniques such as Plasmonic effect through growing nano-antennas on the device surface can be of a choice to improve the device performance.

References

[1] O. Vasan, Ramesh, Makableh, Yahia, Sarker, Jony, and Manasreh, "Enhanced photocurrent due to interband transitions from InAs quantum dots embedded in InGaAs quantum well solar cells," vol. 1551, pp. 0–5, 2013.

[2] H. J. Snaith, "Perovskites: The Emergence of a New Era for Low-Cost, High-Efficiency Solar Cells," *J. Phys. Chem. Lett.*, vol. 4, no. 21, pp. 3623–3630, Nov. 2013.

[3] P. Jackson, D. Hariskos, E. Lotter, S. Paetel, R. Wuerz, R. Menner, W. Wischmann, and M. Powalla, "New world record efficiency for Cu(In,Ga)Se2 thin-film solar cells beyond 20%," *Prog. Photovoltaics Res. Appl.*, vol. 19, no. 7, pp. 894–897, Nov. 2011.

[4] Z. He, C. Zhong, S. Su, M. Xu, H. Wu, and Y. Cao, "Enhanced power-conversion efficiency in polymer solar cells using an inverted device structure," *Nat. Photonics*, vol. 6, no. 9, pp. 593–597, Aug. 2012.

[5] Y. Liu, A. Das, S. Xu, Z. Lin, C. Xu, Z. L. Wang, A. Rohatgi, and C. P. Wong, "Hybridizing ZnO Nanowires with Micropyramid Silicon Wafers as Superhydrophobic High-Efficiency Solar Cells," *Adv. Energy Mater.*, vol. 2, no. 1, pp. 47–51, Jan. 2012.

[6] J. Y. Chen and K. W. Sun, "Growth of vertically aligned ZnO nanorod arrays as antireflection layer on silicon solar cells," *Sol. Energy Mater. Sol. Cells*, vol. 94, no. 5, pp. 930–934, May 2010.

[7] S. L. Diedenhofen, G. Grzela, E. Haverkamp, G. Bauhuis, J. Schermer, and J. G. Rivas, "Broadband and omnidirectional anti-reflection layer for III/V multi-junction solar cells," *Sol. Energy Mater. Sol. Cells*, vol. 101, pp. 308–314, Jun. 2012.

[8] M. a Green, "Third generation photovoltaics: Ultra-high conversion efficiency at low cost," *Prog. Photovoltaics Res. Appl.*, vol. 9, no. 2, pp. 123–135, Mar. 2001.

[9] R. Vasan, Y. F. M. Makableh, J. C. Sarker, and M. O. Manasreh, "Enhanced photocurrent due to interband transitions from InAs quantum dots embedded in InGaAs quantum well solar cells," *MRS Online Proc. Libr.*, vol. 1551, pp. mrss13–1551–r10–03, Jan. 2013.

[10] C. G. Bailey, D. V. Forbes, R. P. Raffaelle, and S. M. Hubbard, "Near 1 V open circuit voltage InAs/GaAs quantum dot solar cells," *Appl. Phys. Lett.*, vol. 98, no. 16, p. 163105, Apr. 2011.

[11] S. M. Hubbard, C. D. Cress, C. G. Bailey, R. P. Raffaelle, S. G. Bailey, and D. M. Wilt, "Effect of strain compensation on quantum dot enhanced GaAs solar cells," *Appl. Phys. Lett.*, vol. 92, no. 12, p. 123512, Mar. 2008.

[12] P. C. Yu, C. H. Chang, C. H. Chiu, C. S. Yang, J. C. Yu, H. C. Kuo, S. H. Hsu, and Y. C. Chang, "Efficiency Enhancement of GaAs Photovoltaics Employing Antireflective Indium Tin Oxide Nanocolumns," *Adv. Mater.*, vol. 21, no. 16, p. 1618–+, Apr. 2009.

[13] G. Wei and S. R. Forrest, "Intermediate-band solar cells employing quantum dots embedded in an energy fence barrier.," *Nano Lett.*, vol. 7, no. 1, pp. 218–22, Jan. 2007.

[14] S. A. Blokhin, A. V. Sakharov, A. M. Nadtochy, A. S. Pauysov, M. V. Maximov, N. N. Ledentsov, A. R. Kovsh, S. S. Mikhrin, V. M. Lantratov, S. A. Mintairov, N. A. Kaluzhniy, and M. Z. Shvarts, "AlGaAs/GaAs photovoltaic cells with an array of InGaAs QDs," *Semiconductors*, vol. 43, no. 4, pp. 514–518, Apr. 2009.

[15] L. Cuadra, A. Marti, and A. Luque, "Influence of the Overlap Between the Absorption Coefficients on the Efficiency of the Intermediate Band Solar Cell," *IEEE Trans. Electron Devices*, vol. 51, no. 6, pp. 1002–1007, Jun. 2004.

[16] A. Luque and A. Martí, "Increasing the Efficiency of Ideal Solar Cells by Photon Induced Transitions at Intermediate Levels," *Phys. Rev. Lett.*, vol. 78, no. 26, pp. 5014–5017, Jun. 1997.

[17] A. Luque, A. Martí, C. Stanley, N. López, L. Cuadra, D. Zhou, J. L. Pearson, and A. McKee, "General equivalent circuit for intermediate band devices: Potentials, currents and electroluminescence," *J. Appl. Phys.*, vol. 96, no. 1, p. 903, Jun. 2004.

[18] G. L. Araújo and A. Martí, "Absolute limiting efficiencies for photovoltaic energy conversion," *Sol. Energy Mater. Sol. Cells*, vol. 33, no. 2, pp. 213–240, Jun. 1994.

[19] G. Medeiros-Ribeiro, D. Leonard, and P. M. Petroff, "Electron and hole energy levels in InAs self-assembled quantum dots," *Appl. Phys. Lett.*, vol. 66, no. 14, p. 1767, Apr. 1995.

[20] K. H. Schmidt, G. Medeiros-ribeiro, J. Garcia, and P. M. Petroff, "Size quantization effects in InAs self-assembled quantum dots," vol. 70, no. November 1996, pp. 1996–1998, 1997.

[21] J. Wu, Y. F. M. Makableh, R. Vasan, M. O. Manasreh, B. Liang, C. J. Reyner, and D. L. Huffaker, "Strong interband transitions in InAs quantum dots solar cell," *Appl. Phys. Lett.*, vol. 100, no. 5, p. 051907, 2012.

[22] K. Nakayama, K. Tanabe, and H. a. Atwater, "Plasmonic nanoparticle enhanced light absorption in GaAs solar cells," *Appl. Phys. Lett.*, vol. 93, no. 12, p. 121904, 2008.

[23] S. Lien, D. Wuu, W. Yeh, and J. Liu, "Tri-layer antireflection coatings (SiO2/SiO2–TiO2/TiO2) for silicon solar cells using a sol–gel technique," *Sol. Energy Mater. Sol. Cells*, vol. 90, no. 16, pp. 2710–2719, Oct. 2006.

[24] Y.-J. Lee, D. S. Ruby, D. W. Peters, B. B. McKenzie, and J. W. P. Hsu, "ZnO nanostructures as efficient antireflection layers in solar cells.," *Nano Lett.*, vol. 8, no. 5, pp. 1501–1505, 2008.

[25] L.-K. Yeh, K.-Y. Lai, G.-J. Lin, P.-H. Fu, H.-C. Chang, C.-A. Lin, and J.-H. He, "Giant Efficiency Enhancement of GaAs Solar Cells with Graded Antireflection Layers Based on Syringelike ZnO Nanorod Arrays," *Adv. Energy Mater.*, vol. 1, no. 4, pp. 506–510, Jul. 2011.

[26] Y. Inomata, K. Fukui, and K. Shirasawa, "Surface texturing of large area multicrystalline silicon solar cells using reactive ion etching method," *Sol. Energy Mater. Sol. Cells*, vol. 48, no. 1–4, pp. 237–242, Nov. 1997.

[27] J. C. Sarker, R. Vasan, Y. F. Makableh, S. Lee, a. I. Nusir, and M. O. Manasreh, "Enhanced performance of surface modified InAs quantum dots solar cell by a sol–gel grown tantalum pentoxide antireflection coating," *Sol. Energy Mater. Sol. Cells*, vol. 127, pp. 58–62, Aug. 2014.

[28] S. Doi, "Enhanced response in InAs quantum dots in an InGaAs quantum well solar cells by anti- reflection coatings Y. F. Makableh, R. Vasan, J. C. Sarker, S. Lee, M. A. Khan and M. O. Manasreh 3217 Bell Engineering Center, University of Arkansas, Fayetteville, AR ," vol. 1551, 2013.

[29] Y. F. Makableh, R. Vasan, J. C. Sarker, A. I. Nusir, S. Seal, and M. O. Manasreh, "Enhancement of GaAs solar cell performance by using a ZnO sol–gel anti-reflection coating," *Sol. Energy Mater. Sol. Cells*, vol. 123, pp. 178–182, 2014.

[30] Y. F. Makableh, R. Vasan, S. Lee, and O. M. Manasreh, "Enhancement of the performance of InAs quantum dots solar cell by surface modification using Poly-L-Lysine homopolymers," *Appl. Phys. Lett.*, vol. 102, no. 5, p. 051904, 2013.

[31] S. Zeng, X. Yu, W.-C. Law, Y. Zhang, R. Hu, X.-Q. Dinh, H.-P. Ho, and K.-T. Yong, "Size dependence of Au NP-enhanced surface plasmon resonance based on differential phase measurement," *Sensors Actuators B Chem.*, vol. 176, pp. 1128–1133, Jan. 2013.

[32] S. Zeng, D. Baillargeat, H.-P. Ho, and K.-T. Yong, "Nanomaterials enhanced surface plasmon resonance for biological and chemical sensing applications.," *Chem. Soc. Rev.*, vol. 43, pp. 3426–52, 2014.

[33] S. Pillai, K. R. Catchpole, T. Trupke, and M. A. Green, "Surface plasmon enhanced silicon solar cells," *J. Appl. Phys.*, vol. 101, no. 9, p. 093105, May 2007.

[34] "Wiley: Solar Cells and Their Applications, 2nd Edition - Lewis M. Fraas, Larry D. Partain." [Online]. Available: http://www.wiley.com/WileyCDA/WileyTitle/productCd-0470446331.html. [Accessed: 05-Mar-2015].

[35] J. J. Loferski, “Theoretical Considerations Governing the Choice of the Optimum Semiconductor for Photovoltaic Solar Energy Conversion,” *J. Appl. Phys.*, vol. 27, no. 7, p. 777, May 1956.

[36] M. A. Green, “Solar cells: operating principles, technology, and system applications,” Jan. 1982.

[37] A. Goetzberger, C. Hebling, and H.-W. Schock, “Photovoltaic materials, history, status and outlook,” *Mater. Sci. Eng. R Reports*, vol. 40, no. 1, pp. 1–46, Jan. 2003.

[38] M. A. Green, K. Emery, Y. Hishikawa, W. Warta, and E. D. Dunlop, “Solar cell efficiency tables (Version 45),” *Prog. Photovoltaics Res. Appl.*, vol. 23, no. 1, pp. 1–9, Jan. 2015.

[39] A. J. Heeger, “25th anniversary article: Bulk heterojunction solar cells: understanding the mechanism of operation.,” *Adv. Mater.*, vol. 26, no. 1, pp. 10–27, Jan. 2014.

[40] G. Conibeer and A. Willoughby, Eds., *Solar Cell Materials*. Chichester, UK: John Wiley & Sons, Ltd, 2014.

[41] W. Shockley and H. J. Queisser, “Detailed balance limit of efficiency of p-n junction solar cells,” *J. Appl. Phys.*, vol. 32, pp. 510–519, 1961.

[42] M. O. Manasreh and O. Manasreh, *Introduction to Nanomaterials and Devices*. John Wiley & Sons, 2012, p. 466.

[43] G. P. Smestad, *Optoelectronics of Solar Cells*. SPIE Press, 2002, p. 99.

[44] *Physics of Solar Cells: From Basic Principles to Advanced Concepts*. John Wiley & Sons, 2009, p. 244.

[45] Z. I. Alexieva, Z. S. Nenova, V. S. Bakardjieva, M. M. Milanova, and H. M. Dikov, “Antireflection coatings for GaAs solar cell applications,” *J. Phys. Conf. Ser.*, vol. 223, no. 1, p. 012045, Apr. 2010.

[46] B.-Y. Su, S.-Y. Chu, Y.-D. Juang, M.-C. Lin, C.-C. Chang, and C.-J. Wu, “Efficiency Enhancement of GaAs Photovoltaics Due to Sol-Gel Derived Anti-Reflective AZO Films,” *J. Electrochem. Soc.*, vol. 159, no. 3, pp. H312–H316, Jan. 2012.

[47] N. D. Arora, “Antireflection layers for GaAs solar cells,” *J. Appl. Phys.*, vol. 53, no. 12, p. 8839, 1982.

[48] L. C.-C. Shen, *Preparation and Properties of Grown Junction GaAs Solar Cells*. Department of Electrical Engineering, Stanford University., 1976, p. 65.

[49] *Thin-Film Solar Cells: Next Generation Photovoltaics and Its Applications*. Springer Science & Business Media, 2004, p. 244.

[50] *Thin Film Solar Cells: Fabrication, Characterization and Applications*. John Wiley & Sons, 2006, p. 502.

[51] B.-Y. Su, S.-Y. Chu, Y.-D. Juang, M.-C. Lin, C.-C. Chang, and C.-J. Wu, "Efficiency Enhancement of GaAs Photovoltaics Due to Sol-Gel Derived Anti-Reflective AZO Films," *J. Electrochem. Soc.*, vol. 159, no. 3, pp. H312–H316, Jan. 2012.

[52] D. T. F. Marple, "Refractive Index of GaAs," *J. Appl. Phys.*, vol. 35, no. 4, p. 1241, 1964.

[53] J. B. Theeten, D. E. Aspnes, and R. P. H. Chang, "A new resonant ellipsometric technique for characterizing the interface between GaAs and its plasma-grown oxide," *J. Appl. Phys.*, vol. 49, no. 12, p. 6097, 1978.

[54] Z. I. Alexieva, Z. S. Nenova, V. S. Bakardjieva, M. M. Milanova, and H. M. Dikov, "Antireflection coatings for GaAs solar cell applications," *J. Phys. Conf. Ser.*, vol. 223, p. 012045, Apr. 2010.

[55] T. Minemoto, T. Mizuta, H. Takakura, and Y. Hamakawa, "Antireflective coating fabricated by chemical deposition of ZnO for spherical Si solar cells," *Sol. Energy Mater. Sol. Cells*, vol. 91, no. 2–3, pp. 191–194, Jan. 2007.

[56] W.-J. Yoon, K.-Y. Jung, J. Liu, T. Duraisamy, R. Revur, F. L. Teixeira, S. Sengupta, and P. R. Berger, "Plasmon-enhanced optical absorption and photocurrent in organic bulk heterojunction photovoltaic devices using self-assembled layer of silver nanoparticles," *Sol. Energy Mater. Sol. Cells*, vol. 94, no. 2, pp. 128–132, Feb. 2010.

[57] J.-L. Wu, F.-C. Chen, Y.-S. Hsiao, F.-C. Chien, P. Chen, C.-H. Kuo, M. H. Huang, and C.-S. Hsu, "Surface plasmonic effects of metallic nanoparticles on the performance of polymer bulk heterojunction solar cells.," *ACS Nano*, vol. 5, no. 2, pp. 959–67, Feb. 2011.

[58] A. J. Morfa, K. L. Rowlen, T. H. Reilly, M. J. Romero, and J. van de Lagemaat, "Plasmon-enhanced solar energy conversion in organic bulk heterojunction photovoltaics," *Appl. Phys. Lett.*, vol. 92, no. 1, p. 013504, Jan. 2008.

[59] K. R. Catchpole and A. Polman, "Plasmonic solar cells," *Opt. Express*, vol. 16, no. 26, p. 21793, Dec. 2008.

[60] D. Derkacs, S. H. Lim, P. Matheu, W. Mar, and E. T. Yu, "Improved performance of amorphous silicon solar cells via scattering from surface plasmon polaritons in nearby metallic nanoparticles," *Appl. Phys. Lett.*, vol. 89, pp. 239–241, 2006.

[61] "This Week ' s Citation," p. 1985, 1985.

[62] C. Powell and J. Swan, “Origin of the Characteristic Electron Energy Losses in Magnesium,” *Phys. Rev.*, vol. 116, no. 1, pp. 81–83, Oct. 1959.

[63] C. Powell and J. Swan, “Origin of the Characteristic Electron Energy Losses in Aluminum,” *Phys. Rev.*, vol. 115, no. 4, pp. 869–875, Aug. 1959.

[64] “Plasmonics: Fundamentals and Applications | Springer.” [Online]. Available: http://www.springer.com/us/book/9780387331508. [Accessed: 08-Mar-2015].

[65] M. Fox, “Optical Properties of Solids,” *Am. J. Phys.*, vol. 70, pp. 1–25, 2001.

[66] “Wiley: Absorption and Scattering of Light by Small Particles - Craig F. Bohren, Donald R. Huffman.” [Online]. Available: http://www.wiley.com/WileyCDA/WileyTitle/productCd-0471293407.html. [Accessed: 09-Mar-2015].

[67] “Classical Electrodynamics : John David Jackson : Free Download & Streaming : Internet Archive.” [Online]. Available: https://archive.org/details/ClassicalElectrodynamics. [Accessed: 09-Mar-2015].

[68] I. Moreno, J. J. Araiza, and M. Avendano-Alejo, “Thin-film spatial filters.,” *Opt. Lett.*, vol. 30, no. 8, pp. 914–916, 2005.

[69] J. Y. Chen and K. W. Sun, “Enhancement of the light conversion efficiency of silicon solar cells by using nanoimprint anti-reflection layer,” *Sol. Energy Mater. Sol. Cells*, vol. 94, no. 3, pp. 629–633, Mar. 2010.

[70] M. H. Kang, K. Ryu, A. Upadhyaya, and A. Rohatgi, “Optimization of SiN AR coating for Si solar cells and modules through quantitative assessment of optical and efficiency loss mechanism,” *Prog. Photovoltaics Res. Appl.*, vol. 19, no. 8, pp. 983–990, Dec. 2011.

[71] X. Zhang, F. Shi, J. Niu, Y. Jiang, and Z. Wang, “Superhydrophobic surfaces: from structural control to functional application,” *J. Mater. Chem.*, vol. 18, no. 6, p. 621, 2008.

[72] P. Roach, N. J. Shirtcliffe, and M. I. Newton, “Progess in superhydrophobic surface development,” *Soft Matter*, vol. 4, no. 2, p. 224, Jan. 2008.

[73] A. Checco, A. Rahman, and C. T. Black, “Robust superhydrophobicity in large-area nanostructured surfaces defined by block-copolymer self assembly.,” *Adv. Mater.*, vol. 26, no. 6, pp. 886–91, Feb. 2014.

[74] B. G. Prevo, Y. Hwang, and O. D. Velev, “Convective Assembly of Antireflective Silica Coatings with Controlled Thickness and Refractive Index,” *Chem. Mater.*, vol. 17, no. 14, pp. 3642–3651, Jul. 2005.

[75] J. Q. Xi, J. K. Kim, E. E. Schubert, D. Ye, T. M. Lu, S.-Y. Lin, and J. S. Juneja, "Very low-refractive-index optical thin films consisting of an array of SiO2 nanorods.," *Opt. Lett.*, vol. 31, no. 5, pp. 601–3, Mar. 2006.

[76] X. Y. Ling, I. Y. Phang, G. J. Vancso, J. Huskens, and D. N. Reinhoudt, "Stable and transparent superhydrophobic nanoparticle films.," *Langmuir*, vol. 25, no. 5, pp. 3260–3, Mar. 2009.

[77] S. Wang and L. Jiang, "Definition of Superhydrophobic States," *Adv. Mater.*, vol. 19, no. 21, pp. 3423–3424, Nov. 2007.

[78] T. Young, "An Essay on the Cohesion of Fluids," *Philos. Trans. R. Soc. London*, vol. 95, no. January, pp. 65–87, 1805.

[79] W. Haiss, N. T. K. Thanh, J. Aveyard, and D. G. Fernig, "Determination of size and concentration of gold nanoparticles from UV-vis spectra.," *Anal. Chem.*, vol. 79, no. 11, pp. 4215–21, Jun. 2007.

[80] L. Mulfinger, S. D. Solomon, M. Bahadory, A. V. Jeyarajasingam, S. A. Rutkowsky, and C. Boritz, "Synthesis and Study of Silver Nanoparticles," *J. Chem. Educ.*, vol. 84, no. 2, p. 322, Feb. 2007.

[81] O. Tari, A. Aronne, M. Luisa, S. Daliento, E. Fanelli, and P. Pernice, "Solar Energy Materials & Solar Cells Sol – gel synthesis of ZnO transparent and conductive films : A critical approach," vol. 105, pp. 179–186, 2012.

[82] S. Ilican, Y. Caglar, and M. Caglar, "Preparation and characterization of ZnO thin films deposited by sol-gel spin coating method," vol. 10, no. 10, pp. 2578–2583, 2008.

[83] J. Jean, S. Chang, P. R. Brown, J. J. Cheng, P. H. Rekemeyer, M. G. Bawendi, S. Gradečak, and V. Bulović, "ZnO nanowire arrays for enhanced photocurrent in PbS quantum dot solar cells," *Adv. Mater.*, vol. 25, pp. 2790–2796, 2013.

[84] G. Sauthier, J. J. Segura, J. Fraxedas, and A. Verdaguer, "Hydrophobic coating of mica by stearic acid vapor deposition," *Colloids Surfaces A Physicochem. Eng. Asp.*, vol. 443, pp. 331–337, Feb. 2014.

[85] J. Gao, Y. Li, Y. Li, H. Liu, and W. Yang, "Fabrication of superhydrophobic surface of stearic acid grafted zinc by using an aqueous plasma etching technique," *Cent. Eur. J. Chem.*, vol. 10, no. 6, pp. 1766–1772, Sep. 2012.

[86] M. Guo, P. Diao, and S. Cai, "Hydrothermal growth of well-aligned ZnO nanorod arrays: Dependence of morphology and alignment ordering upon preparing conditions," *J. Solid State Chem.*, vol. 178, pp. 1864–1873, 2005.

[87] T. H. Meen, W. Water, Y. S. Chen, W. R. Chen, L. W. Ji, and C. J. Huang, "Growth Of ZnO Nanorods by Hydrothermal Method Under Different Temperatures," pp. 617–620, 2007.

[88] Y. S. Bae, D. C. Kim, C. H. Ahn, J. H. Kim, and H. K. Cho, "Growth of ZnO nanorod arrays by hydrothermal method using homo-seed layers annealed at various temperatures," *Surface and Interface Analysis*, vol. 42. pp. 978–982, 2010.

[89] D. Polsongkram, P. Chamninok, S. Pukird, L. Chow, O. Lupan, G. Chai, H. Khallaf, S. Park, and a. Schulte, "Effect of synthesis conditions on the growth of ZnO nanorods via hydrothermal method," *Phys. B Condens. Matter*, vol. 403, pp. 3713–3717, 2008.

[90] S. Xu, Y. Ding, Y. Wei, H. Fang, Y. Shen, A. K. Sood, D. L. Polla, and L. W. Zhong, "Patterned growth of horizontal ZnO nanowire arrays," *J. Am. Chem. Soc.*, vol. 131, pp. 6670–6671, 2009.

[91] R. Heryanto, M. Hasan, E. C. Abdullah, and A. C. Kumoro, "Solubility of stearic acid in various organic solvents and its prediction using non-ideal solution models," *ScienceAsia*, vol. 33, pp. 469–472, 2007.

[92] X. J. Shang, J. F. He, H. L. Wang, M. F. Li, Y. Zhu, Z. C. Niu, and Y. Fu, "Effect of built-in electric field in photovoltaic InAs quantum dot embedded GaAs solar cell," *Appl. Phys. A*, vol. 103, no. 2, pp. 335–341, Dec. 2010.

[93] D. M. Schaadt, B. Feng, and E. T. Yu, "Enhanced semiconductor optical absorption via surface plasmon excitation in metal nanoparticles," *Appl. Phys. Lett.*, vol. 86, pp. 1–3, 2005.

[94] I. Calizo, K. a. Alim, V. a. Fonoberov, S. Krishnakumar, M. Shamsa, A. a. Balandin, and R. Kurtz, "Micro-Raman spectroscopic characterization of ZnO quantum dots, nanocrystals and nanowires," *Proc. SPIE*, vol. 6481, p. 64810N–64810N–8, 2007.

[95] Z. R. Khan, "Optical and Structural Properties of ZnO Thin Films Fabricated by Sol-Gel Method," *Mater. Sci. Appl.*, vol. 02, no. May, pp. 340–345, 2011.